Structural Elucidation of Viral Antagonism of Innate Immunity at the STAT1 Interface

Md Alamgir Hossain, Florence Larrous, Stephen Rawlinson, Jingyu Zhan, Ashish Sethi, Youssef Ibrahim, Maria Aloi, Kim Lieu, Yee-Foong Mok, Michael Griffin, et al.

Article

Cell Reports

Structural Elucidation of Viral Antagonism of Innate Immunity at the STAT1 Interface

Graphical Abstract

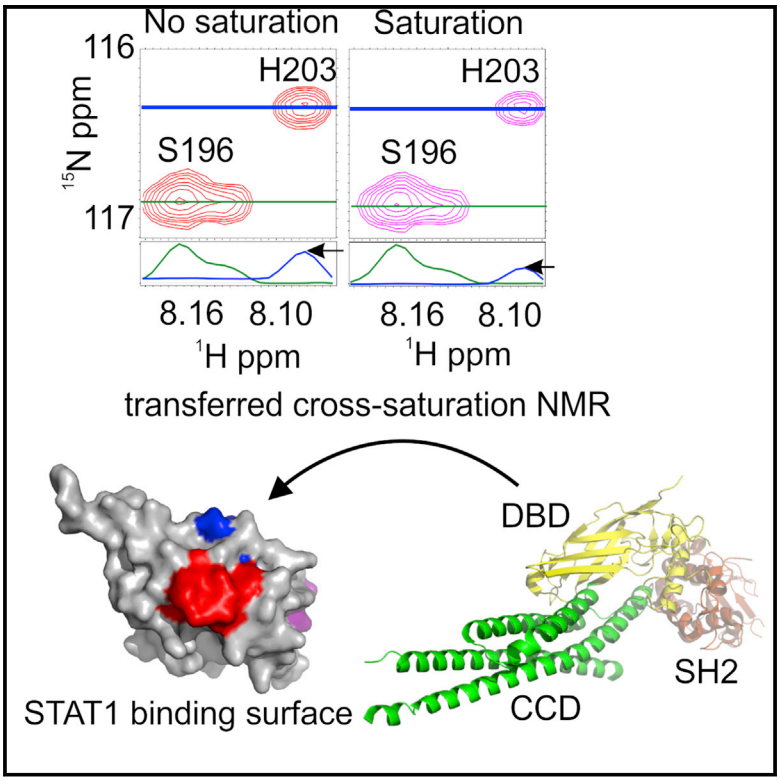

Highlights

- Elucidation of the interface of full-length STAT1 and a viral interferon antagonist
- The viral protein-STAT1 interface involves multiple distinct surfaces
- Ablation of the interaction requires multiple mutations at distinct sites
- Loss of viral protein-STAT1 interaction attenuates a rabies virus street strain

Authors

Md. Alamgir Hossain, Florence Larrous, Stephen M. Rawlinson, ..., Hervé Bourhy, Gregory W. Moseley, Paul R. Gooley

Correspondence

greg.moseley@monash.edu (G.W.M.), prg@unimelb.edu.au (P.R.G.)

In Brief

Hossain et al. explore the binding surface of the multifunctional P-protein of rabies virus for STAT1, a protein that is essential for establishing the antiviral response of infected cells. They identify a complex interface comprising several distinct sites and demonstrate that targeted modifications of these can significantly attenuate pathogenic virus.

Hossain et al., 2019, Cell Reports *29*, 1934–1945
November 12, 2019
https://doi.org/10.1016/j.celrep.2019.10.020

CellPress

OPEN ACCESS
CellPress

Cell Reports
Article

Structural Elucidation of Viral Antagonism of Innate Immunity at the STAT1 Interface

Md. Alamgir Hossain,[1] Florence Larrous,[2,3,7] Stephen M. Rawlinson,[4,7] Jingyu Zhan,[1,7] Ashish Sethi,[1] Youssef Ibrahim,[1] Maria Aloi,[4] Kim G. Lieu,[4] Yee-Foong Mok,[1] Michael D.W. Griffin,[1] Naoto Ito,[5] Toyoyuki Ose,[6] Hervé Bourhy,[2,3] Gregory W. Moseley,[1,4,8,*] and Paul R. Gooley[1,8,9,*]

[1]Department of Biochemistry and Molecular Biology, University of Melbourne, Parkville, VIC 3010, Australia
[2]Bio21 Molecular Science and Biotechnology Institute, University of Melbourne, Parkville, VIC 3010, Australia
[3]Unité Lyssavirus, Epidémiologie et Neuropathologie - CNR de la RAGE, Institut Pasteur, 25 rue du Dr. Roux, 75724 Paris Cedex 15, France
[4]Department of Microbiology, Biomedicine Discovery Institute, Monash University, Clayton Campus, VIC 3800, Australia
[5]Laboratory of Zoonotic Diseases, Joint Department of Veterinary Medicine, Faculty of Applied Biological Sciences, Gifu University, 1-1 Yanagido, Gifu 501-1193, Japan
[6]Faculty of Advanced Life Science, Hokkaido University, 060-0810 Sapporo, Japan
[7]These authors contributed equally
[8]These authors contributed equally
[9]Lead Contact
*Correspondence: greg.moseley@monash.edu (G.W.M.), prg@unimelb.edu.au (P.R.G.)
https://doi.org/10.1016/j.celrep.2019.10.020

SUMMARY

To evade immunity, many viruses express interferon antagonists that target STAT transcription factors as a major component of pathogenesis. Because of a lack of direct structural data, these interfaces are poorly understood. We report the structural analysis of full-length STAT1 binding to an interferon antagonist of a human pathogenic virus. The interface revealed by transferred cross-saturation NMR is complex, involving multiple regions in both the viral and cellular proteins. Molecular mapping analysis, combined with biophysical characterization and *in vitro/in vivo* functional assays, indicates that the interface is significant in disease caused by a pathogenic field-strain lyssavirus, with critical roles for contacts between the STAT1 coiled-coil/DNA-binding domains and specific regions within the viral protein. These data elucidate the potentially complex nature of IFN antagonist/STAT interactions, and the spatial relationship of protein interfaces that mediate immune evasion and replication, providing insight into how viruses can regulate these essential functions via single multifunctional proteins.

INTRODUCTION

The type I interferon (IFN) system comprises the earliest response of host cells against viral infection (Nan et al., 2017; Randall and Goodbourn, 2008; Versteeg and García-Sastre, 2010). Following infection, cells release IFNs that bind type I IFN receptors to activate the signal transducers and activators of transcription (STAT) family members STAT1 and STAT2 via phosphorylation of conserved tyrosines. This results in activation of IFN-stimulated genes (ISGs), products of which include antiviral and immunomodulatory proteins that establish an antiviral state and facilitate adaptive responses.

In resting cells, STATs are generally unphosphorylated (U-STAT) antiparallel dimers, but following activation phosphorylated STATs (pY-STAT) form parallel dimers that enter the nucleus to activate ISGs (Lim and Cao, 2006). pY-STAT1/2 are the major mediators of type I IFN signaling. Within the nucleus, pY-STAT1/2 complexes with IFN-regulatory factor 9 (IRF9) bind to IFN-stimulated response elements (ISREs) in ISG promoters. pY-STAT1 homodimers are also activated by type I IFN, and bind distinct γ-activated sequences (GASs). Although pY-STAT signaling has formed the focus of research, U-STATs also mediate gene transcription relevant to immunity, cell proliferation, and cancer (Cheon et al., 2013; Yang and Stark, 2008).

Viruses have numerous strategies to overcome the IFN response, mediated principally by viral IFN antagonist proteins. Given their central roles in responses to cytokines including IFNs, it is not surprising that many IFN antagonists interfere with STATs, especially STAT1 by diverse mechanisms (Audsley and Moseley, 2013; Ito et al., 2016; Nan et al., 2017; Versteeg and García-Sastre, 2010). Because of the importance of IFN in controlling infections, it has been assumed that mechanisms of IFN antagonism play essential roles in pathogenesis (Fensterl and Sen, 2009; Versteeg and García-Sastre, 2010). Studies using recombinant viruses defective in specific IFN antagonist mechanisms are limited, but an analysis of rabies virus (RABV) and measles virus (Devaux et al., 2011; Wiltzer et al., 2014) containing mutations inhibiting IFN antagonist/STAT1 interaction indicated important roles, suggesting that this interface could provide targets for antiviral drugs or vaccine development. However, the precise nature of the interaction sites remains largely unresolved because of a lack of direct structural data on

STAT1 complexes with viral proteins; thus, most data come from mutagenic studies, interpretation of which is particularly difficult for multifunctional viral proteins.

P-protein is the main IFN antagonist of lyssaviruses, which comprise a genus of highly pathogenic viruses, including RABV that causes rabies with a case fatality rate of ~100% (Ito et al., 2016). In common with many other IFN antagonists, P-protein targets both IFN induction and signaling (Brzózka et al., 2005; Ito et al., 2016). The latter involves interaction with STAT1 (Vidy et al., 2005; Wiltzer et al., 2012), which was originally identified by yeast-two-hybrid analysis, suggesting a direct interaction, and causes mislocalization of pY-STAT1 out of nuclei via nuclear export and cytoskeletal association of P-protein isoforms (Brice and Moseley, 2013; Ito et al., 2010; Moseley et al., 2009; Wiltzer et al., 2012). Using recombinant RABV containing mutated P-protein, these antagonistic mechanisms were correlated with pathogenicity (Brice et al., 2016; Ito et al., 2010, 2016; Wiltzer et al., 2014). P-protein is also an essential replication co-factor via interaction with nucleocapsid (N) protein associated with genomic RNA (N-RNA) and the polymerase (L-protein). Thus, P-protein is a complex multifunctional protein.

The globular C-terminal domain of P-protein (P-CTD) contains sites required for binding to STAT1 (Vidy et al., 2005; Wiltzer et al., 2014) and N-RNA (Schoehn et al., 2001) and so is central to replication and immune evasion functions. Despite this, the molecular details of P-CTD interactions are poorly understood. The X-ray crystal structure was solved (Mavrakis et al., 2004), and a model based on small-angle X-ray scattering (SAXS) data of the P-CTD/N-RNA complex was proposed (Ribeiro Ede et al., 2009). Yeast-two-hybrid experiments suggested that P-protein binds to the coiled-coil domain (CCD) and DNA-binding domain (DBD) region (CCD-DBD) of STAT1. Subsequent analysis of endogenous STAT1 in mammalian cell lysates with DNA probes containing STAT1-target sequences indicated that STAT1/DNA interaction can be inhibited by RABV infection or presence of full-length P-protein or its isoforms (Vidy et al., 2005, 2007). This suggests that P-CTD/STAT1-DBD interaction might compete with DNA; however, the minimal STAT1-binding region, P-CTD, has not been shown to be sufficient for inhibition of DNA interaction. Furthermore, confirmation that purified P-CTD and STAT1 interact, and that this directly inhibits STAT1-DNA binding in a cell-free system, has not been reported.

Recently, mutagenesis on the basis of sequence and functional analysis of P-proteins of different lyssaviruses indicated that changes to the "W-hole," a hydrophobic cleft of P-CTD, can inhibit STAT1 interaction and thereby generate a viable but highly IFN-sensitive and attenuated RABV (Wiltzer et al., 2014). Although these data suggest a role for the W-hole in the interface, this has not been demonstrated, and there is no direct structural data on any P-CTD complex.

In this study we use NMR spectroscopy to elucidate the STAT1-binding interface on P-CTD. Results indicate that the P-CTD/STAT1 complex comprises a discrete intermolecular interaction, by which P-CTD disrupts pY-STAT1/DNA binding. However, the interface did not include the W-hole and rather is extended, comprising several distinct regions in P-CTD that contact different STAT1 domains, indicating that IFN antagonist/STAT complexes can involve extensive interfaces. Consistent with this, ablation of the interaction and antagonism of STAT1/DNA binding/transcriptional activation required multiple mutations of different regions of P-CTD. The new mutations did not affect the fitness of a street strain virus *in vitro* but caused attenuation *in vivo*.

RESULTS

Expression, Purification, and Characterization of STAT1

Structural studies of STAT1 often use truncated protein (Oda et al., 2015), perhaps reflecting expression and purification difficulties for full-length protein. To assess P-CTD/STAT1 interaction, we initially expressed full-length STAT1 as a glutathione S-transferase (GST) fusion. After purification and removal of GST, the yield was ~2 mg with aggregates of >50% eluting in the void volume of size exclusion chromatography (SEC) (Figure S1A). Furthermore, the purified protein almost immediately commenced precipitation at room temperature or within 8 h at 4°C, indicating poor stability.

We thus tested the GB1 fusion tag as a solubility enhancer (Zhou and Wagner, 2010). STAT1 and a truncate comprising the CCD-DBD expressed with N-terminal GB1- and C-terminal His_6 tags showed that >80% of protein was in the soluble fractions after lysis, with yields after purification of ~30 mg/L of culture. SEC showed little aggregation (Figure S1A); therefore the GB1 tag markedly enhances STAT1 expression, stability, and solubility, enabling >15-fold improvement in yield.

To assess the structural integrity of GB1-STAT1 or GB1-CCD-DBD, we used circular dichroism (CD) to show that the proteins were correctly folded (Figure S1C), with experimental secondary structure values fitting well with those calculated (Figure S1D). Sedimentation coefficient distributions *c*(*s*) from sedimentation velocity analytical ultracentrifugation (SV-AUC) indicated that GB1-STAT1 (Figure S2A) forms one major and two minor species; the major peak had a weight average coefficient of ~6.5 S, corresponding to an expected dimer, and an estimated molecular weight of 187 kDa (theoretical mass 191 kDa) (Mao et al., 2005; Wenta et al., 2008). The minor peaks (~3.7 S, ~9.5 S) likely correspond to monomeric and multimeric STAT1. Sedimentation coefficients for GB1-CCD-DBD (Figure S2B) identified a major species with a sedimentation coefficient of ~2.9 S, corresponding to a monomer, and an estimated molecular weight of 49 kDa (theoretical mass 50 kDa), consistent with the absence of the N-terminal domain (ND), which stabilizes U-STAT1 dimerization (Wenta et al., 2008). The frictional ratios for GB1-STAT (1.7) and GB1-CCD-DBD (1.5) suggest asymmetrical, elongated shapes.

Direct interaction of P-CTD and STAT1 was suggested by yeast-two-hybrid experiments (Vidy et al., 2005), although subsequent analyses have relied on microscopy or co-immunoprecipitation (coIP) using mammalian cells. To determine whether P-CTD/STAT1 interact directly in the absence of other cellular factors, and examine the molecular basis of such complexes, we expressed and purified the P-CTD of the Nishigahara RABV strain, tagged with GFP. Fluorescence-detected SV-AUC (FDS-AUC) experiments on GFP-P-CTD titrated with non-fluorescent GB1-STAT1 (Figure S2C) reveal a new peak at ~7.4 S, attributed to a GFP-P-CTD/GB1-STAT1 complex. Titration using

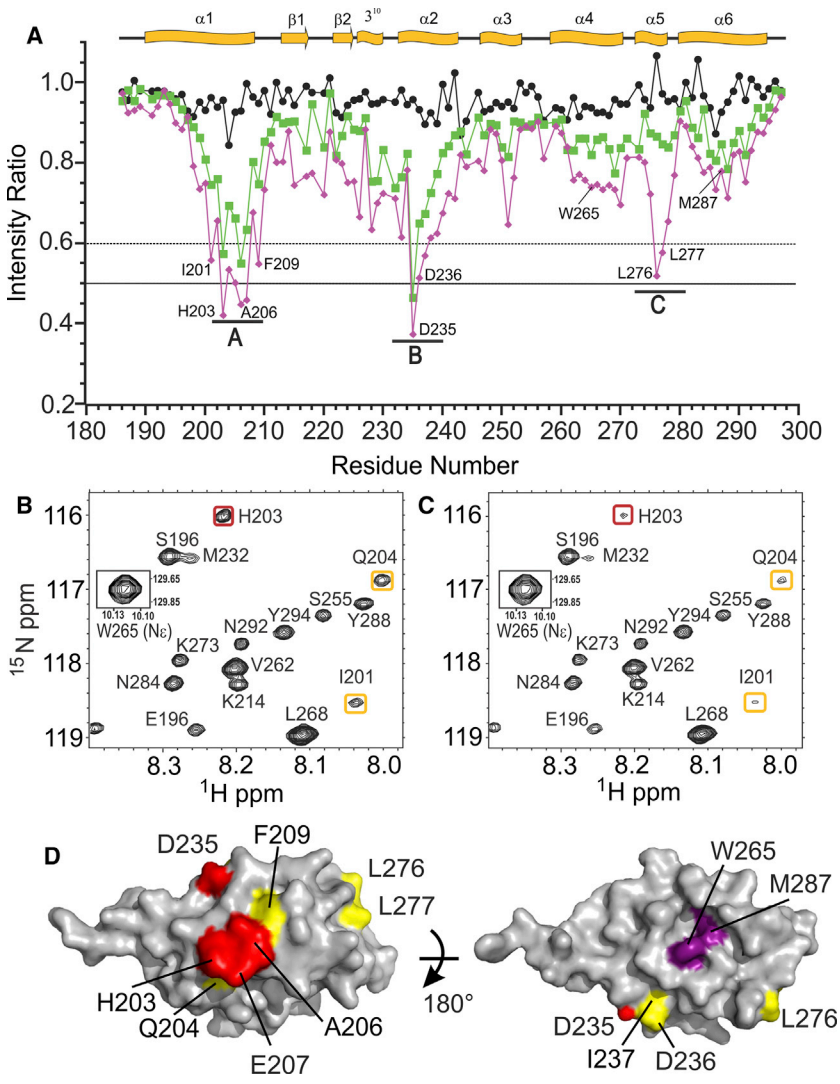

Figure 1. Identification of STAT1-Binding Sites on P-CTD

(A) Intensity ratios of NH resonances from on- and off-resonance saturation ^{15}N, ^{1}H transverse relaxation-optimized spectroscopy (TROSY) of $^{15}N,^{2}H$ P-CTD plotted against residue number and secondary structure for apo-P-CTD (no STAT1, black), in the presence of GB1-STAT1 (magenta), and GB1-CCD-DBD (green). With GB1-STAT1, intensity for H203, I205, A206, E207, and D235 reduces to <0.5 (unbroken line) and for I201, Q204, F209, D236, I237, L276, and L277 reduces to within 0.6–0.5 (dashed line). Residues contributing to interactions lie within helices 1, 2, and 5 of P-CTD. W265 and M287 are indicated.

(B and C) Examples of intensities of cross-peaks of P-CTD in the presence of GB1-STAT1: (B) off-resonance and (C) on-resonance saturation. Intensities reduced >0.5 (red boxes) or within 0.6–0.5 (yellow boxes) are indicated. Insets in (B) and (C) show that N$^{\varepsilon}$H of W265 is not attenuated.

(D) Surface representations of residues significantly attenuated with GB1-STAT1 (<0.5 in red, 0.6–0.5 in yellow) and residues of the W-hole (purple) mapped onto CVS P-CTD structure (PDB: 1VYI), viewing the round (left panel) and flat faces (right panel).

GB1-CCD-DBD (Figure S2D) revealed a decrease of the GFP-P-CTD peak and appearance of a new species at ~3.7 S. Thus, the proteins interact directly; assuming 1:1 binding, and accounting for peak volumes of free and complexed GFP-P-CTD, we estimate an affinity (K_D) of ~10–20 μM.

Mapping the STAT1 Interaction Site on P-CTD

The above data are consistent with studies indicating that the STAT1-binding site is in the P-CTD (Vidy et al., 2005; Wiltzer et al., 2014), and provide evidence that this involves a discrete interaction with the CCD-DBD. As the AUC experiments showed P-CTD binds weakly to U-STAT1, we acquired transferred cross-saturation NMR data using $^{15}N,^{2}H$ P-CTD and $^{14}N,^{1}H$ GB1-STAT1 or GB1-CCD-DBD (Figure 1). Three regions of P-CTD were attenuated with GB1-STAT1: I201-F209 *(region A)*, D235-K237 (region B) and L276-V277 (*region C*), suggesting an extended interface, but with GB1-CCD-DBD, only resonances from regions A and B were attenuated. Previous studies using cell lysates indicated that RABV or P-protein can suppress interaction of endogenous STAT1 with DNA probes (Vidy et al., 2007), potentially via direct interaction at the CCD-DBD. Our data support direct bi-molecular interaction at this site, and indicate specific regions (A/B) in P-CTD form this interface, enabling direct assessment of their functional importance.

Residues of all regions are highly conserved among lyssaviruses (Figure S3). Regions A and B are distant in the sequence, but proximal in the folded domain. Nevertheless, they are likely to form quite distinct interactions with the CCD-DBD, as region A sits centrally in the round face, and region B sits on the edge of the round and flat faces, so that side chains of residues of region B point in the opposite direction to those of region A (Figure 1D). Region C is distant from regions A/B and does not contact the CCD-DBD, suggestive of alternative roles or contribution to overall binding affinity. Previous experiments indicated that mutation of W-hole residues W265G/M287V inhibit binding and antagonism of STAT1, and viral pathogenesis (Wiltzer et al., 2014), suggesting the W-hole might form part of the binding site. The W-hole sits centrally in the flat face, on the opposite side to region A, and distant from regions B and C. Our data, including the lack of any attenuation of N$^{\varepsilon}$H of W265 (Figure 1C), indicate that binding does not directly involve the W-hole.

Mutational Analysis of the Interface

To examine roles of regions A, B and C in antagonizing STAT1-mediated transcription, point mutations were introduced into full-length Nishigahara P-protein (Ni-P) and antagonism of cellular IFN-STAT1 signaling assessed using a reporter assay

Table 1. STAT1 Antagonism by Mutant P-proteins

P-protein	−IFN	+IFN	% Soluble[a]
Controls			
CVS WT	0.3 ± 0.1 (2)	3.8 ± 0.3 (2)	ND
CVS PΔ30	0.3 ± 0.1 (6)	100 (6)	ND
Ni-P WT	0.2 ± 0.1 (6)	3.1 ± 1.8 (6)	90
Ni-P; Single Mutants			
H203A	0.1	2.2	90
Q204A	0.1	2.0	ND
A206G	0.3 ± 0.1 (2)	2.3 ± 0.5 (2)	90
A206E	0.2 ± 0.1 (3)	6.1 ± 1.6 (3)	90
E207A	0.1	1.8	ND
F209A	0.3 ± 0.1 (4)	35.8 ± 6.0 (4)	70
D235A	0.4 ± 0.1 (3)	11.3 ± 4.1 (3)	90
D235K	0.3 ± 0.2 (3)	13.6 ± 5.8 (3)	90
D236A	0.3 ± 0.2 (2)	3.5 ± 0.1 (2)	90
K239A	0.20	2.4	ND
W265G	0.3 ± 0.1 (4)	11.9 ± 3.1 (4)	60
L277A	0.2	2.9	ND
L276A	0.2	1.0 ± 0.1 (2)	ND
L276E	0.1	1.8 ± 0.1 (2)	ND
M287V	0.3 ± 0.1 (4)	10.7 ± 1.9 (4)	70
Ni-P; Double Mutants			
F209A/D235A	0.5 ± 0.3 (3)	96.1 ± 6.4 (3)	80
A206E/D235K	0.2 ± 0.1 (3)	62.0 ± 6.5 (3)	90
D235A/D236A	0.2	29.3 ± 3.0 (2)	90
L276E/L277E	0.1	1.5 ± 0.3 (2)	ND
L276A/L277A	0.1	1.7 ± 0.1 (2)	ND
W265G/M287V	0.3 ± 0.2 (3)	81.0 ± 2.0 (3)	10

Results of screens using an IFN-dependent luciferase reporter assay to assess antagonist function of the indicated P-proteins expressed in HEK293-T cells treated without (−) or with (+) IFN. Data are from multiple screens, so normalized luciferase activity is shown as a percentage of the internal positive control for each assay (IFNα-treated CVS PΔC30-expressing cells). Data from each individual assay are the mean of triplicates; where multiple assays were performed, n values (in parentheses) indicate the number of biological replicates used to calculate mean ± SD. ND, not done.
[a]Solubility of P-CTD expressed from *E. coli*.

as previously described (Vidy et al., 2005; Wiltzer et al., 2012, 2014). Ten residues (Table 1) were selected on the basis of the degree of attenuation of resonances and surface exposure (Figure 1). Controls included wild-type (WT) P-protein of CVS RABV (CVS-P), which strongly antagonizes STAT1, and CVS-P deleted for the C-terminal 30 residues (PΔ30), a standard control deficient in STAT1 targeting and replication function (Vidy et al., 2005; Wiltzer et al., 2014). As expected, WT Ni-P suppressed IFN signaling (indicated by reduction of IFN-dependent induction of luciferase to ~3% of that observed for PΔ30), while Ni-P containing W-hole mutations W265G and M287V, previously shown to impair antagonism by CVS-P, was clearly defective (Table 1).

Analysis of single mutations indicated modest effects for F209A (~36% that for PΔ30), D235A and D235K (~11%–14%), and A206E (~6%). As shown for CVS-P (Wiltzer et al., 2014), Ni-P containing W265G or M287V alone was partially defective (~11%). Other single mutations showed little to no evident impact (Table 1). Mutations altering size, polarity, or charge (D235K, L276E) did not substantially differ from alanine mutations, although A206E appeared moderately defective compared with A206G, which had no apparent impact (Table 1). Dual mutation of surface residues of region A (D235/D236) had a greater effect than single mutants, but this remained moderate (~29%), whereas mutation of L276/L277 of region C gave no clear effect. These data indicate that discrete changes to individual regions are insufficient to strongly suppress STAT1 antagonism, consistent with interaction via multiple contacts. Nevertheless, certain mutations in region A or B could partially reduce antagonism of STAT transcriptional function, perhaps consistent with roles in binding the CCD-DBD, supporting a key role of this interaction in immune evasion (Vidy et al., 2005). Although region C is clearly attenuated by full-length STAT1, mutations to this region were not sufficient to significantly affect transcriptional inhibition in this screen, consistent with region C binding outside of the CCD-DBD and unlikely to affect DNA binding. Thus, region C may play different roles in STAT1 targeting and/or represent a minor binding site for the N- or C-terminal regions of the same STAT1 protein bound by region A/B, or for a site within the opposing monomer of dimeric STAT1, as dimerization is not possible for the CCD-DBD truncate because of the absence of the ND (Wenta et al., 2008).

On the basis of the data indicating significance of regions A and B, we analyzed effects of mutations affecting both regions, combining mutants that had partial effects individually. A206E/D235K produced a substantially greater effect than either mutation alone (62%), while F209A/D235A ablated antagonism (96%) (Table 1); importantly, western analysis of lysates indicated that defects caused by these mutations are not due to altered P-protein expression (Figure S4). The potent effect of mutations affecting both regions compared with changes to individual regions is consistent with the extensive interface predicted using NMR.

Notably, despite a substantial effect of W265G/M287V, it retained some antagonist function (81% that of PΔ30), and we consistently observed a significantly greater defect by F209A/D235A ($p = 0.0175$, Student's t test). These data suggest that the latter mutations have more potent impact on STAT1 interaction, consistent with their placement within predicted binding regions. F209A/D235A was thus selected for further analysis.

F209A/D235A Mutation Prevents P-CTD-STAT1 Interaction

To confirm that the effect of F209A/D235A on STAT1 antagonism was due to altered binding, we tested interaction of the isolated P-CTD and STAT1 proteins *in vitro* using NMR. A two-dimensional (2D) $^{15}N,^{1}H$ heteronuclear single quantum coherence (HSQC)-monitored titration of ^{15}N-WT P-CTD with equimolar GB1-STAT1 resulted in an average of 52% loss of resonance intensity for 88 well-resolved peaks (Figure 2A). Despite relatively strong inhibitory effects on antagonist function of P-protein in signaling assays (Table 1), W265G/M287V P-CTD produced similar broadening patterns to WT (average 41% loss of

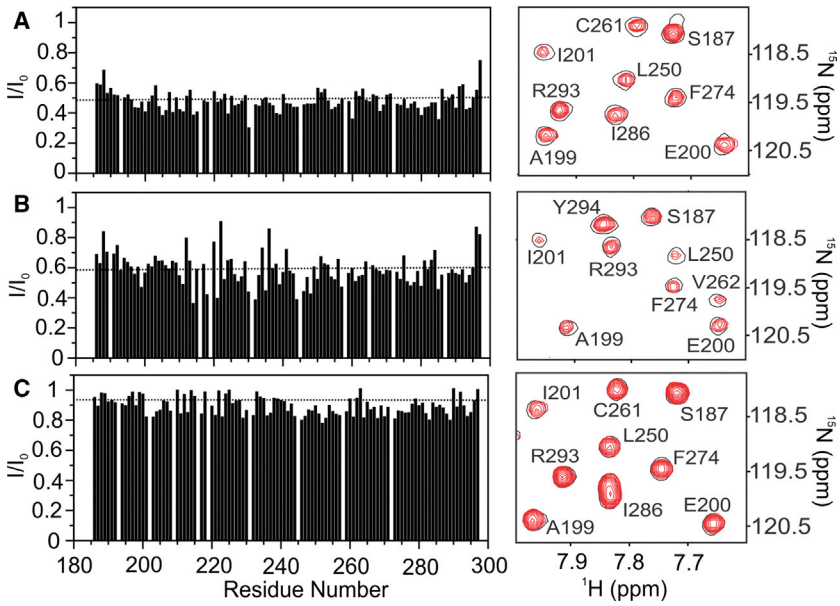

Figure 2. F209A/D235A Ablates P-CTD Binding to STAT1

(A–C) WT (A), W265G/M287V (B), and F209A/D235A (C) ^{15}N-P-CTD (30 μM) titrated with GB1-STAT1 (30 μM); intensity differences are shown in histograms. Portions of ^{15}N,^{1}H HSQC spectra for P-CTD proteins with (multiple contours, red) and without (single contour, black) GB1-STAT1. Spectra are plotted at the same levels.

intensity, 83 peaks) (Figure 2B). In contrast, F209A/D235A P-CTD produced little broadening (average 7% loss of intensity, 85 peaks) (Figure 2C). Thus, although W265G/M287V reduces STAT1 binding, F209A/D235A lacks detectable binding, consistent with the data indicating that regions A and B are critical (Table 1).

To confirm that effects on isolated protein interactions correlate with interactions in cells, we used coIP and confocal laser scanning microscopy (CLSM) analysis. The original identification of P-protein/STAT1 interaction (Vidy et al., 2005) indicated that STAT1-CCD-DBD is sufficient to mediate binding in the absence of activation by tyrosine phosphorylation, as the tyrosine is in the transactivation domain (TAD; Figure S1B). However, several studies show that efficient interaction detected by coIP from cells requires IFN activation (Brzózka et al., 2006; Wiltzer et al., 2012). Consistent with this, WT Ni-P, but not PΔ30, co-precipitated STAT1 from cells treated with IFN for 0.5 h (Figure 3A) (Wiltzer et al., 2012, 2014). In agreement with the lack of antagonistic function and binding in NMR, Ni-P F209A/D235A replicated the phenotype of PΔ30, showing no detectable interaction (Figure 3A, IP: lane FD).

CLSM analysis (Figure S5) of the localization of immunostained STAT1 in cells expressing GFP-fused WT and mutant Ni-P indicated that, as expected, STAT1 rapidly accumulated into nuclei following IFN activation (0.5 h), and this was prevented by WT Ni-P (Ito et al., 2010). Consistent with complete loss of STAT1 antagonism, F209A/D235A Ni-P did not inhibit STAT1 nuclear translocation.

Our data indicate that W265G/M287V retains significant capacity to bind STAT1 *in vitro* (Figure 2) but is strongly defective in antagonism of IFN/STAT1 signaling in cells (Table 1; Figure 3A). Consistent with retention of binding, at least at early time points (0.5 h) of IFN treatment, W265G/M287V Ni-P suppressed IFN-dependent STAT1 nuclear translocation (Figure S5). coIP assays also indicated W265G/M287V Ni-P interacted with STAT1 at 0.5–1 h IFN treatment when cellular pY-STAT1 levels are maximal (Figure 3A); however, in multiple assays, binding was clearly reduced compared with WT Ni-P. Furthermore, although WT Ni-P retained STAT1 binding over extended periods (>16 h, as expected; Wiltzer et al., 2014), binding was lost for W265G/M287V. P-protein causes cytosolic accumulation of pY-STAT1 in cells, most likely because of retention in antagonistic complexes that prevent dephosphorylation by nuclear phosphatases, which ordinarily occurs from 0.5–1 h IFN treatment as a negative regulatory mechanism (Brzózka et al., 2006; Wiltzer et al., 2012) (Figure 3A, input lanes). Thus P-protein prevents normal phosphorylation/dephosphorylation recycling (Brzózka et al., 2006), which presumably enables sustained antagonism. Our data indicate that W265G/M287V Ni-P is defective both for initial binding affinity and for retention of pY-STAT1 (Figure 3A), accounting for defective antagonism. Nevertheless, it clearly has residual STAT1 interaction compared with F209A/D235A Ni-P, explaining incomplete loss of antagonist function (Table 1). As the NMR data indicate that W265 and M287 are not a part of the binding region, the effects of the mutations are likely indirect via conformational effects. In contrast, F209A/D235A Ni-P is as potent as PΔ30, consistent with specific removal of critical STAT1 contacts.

Structural Analysis of Mutated P-CTD

To assess conformational effects of F209A/D235A or W265G/M287V, we purified P-CTD containing single or double mutants. Although all single mutants and F209A/D235A expressed as soluble proteins (>60%) (Table 1), W265G/M287V expressed largely into the pellet fraction (10% in the lysis supernatant), consistent with the idea that defective STAT1 antagonism may be due to loss of proper folding. We next ^{13}C, ^{15}N labeled WT and mutant P-CTD, assigned the ^{15}N, NH, ^{13}Cα, ^{13}Cβ, and C′ resonances, and assessed secondary structure differences. Secondary structure of WT was consistent with the crystal structure of CVS P-CTD (Mavrakis et al., 2004), and there were no significant differences between WT and mutant proteins (Figure 4A). However, comparison of the ^{1}H-^{15}N average chemical shifts of mutant and WT proteins (Figure 4C) showed that, in addition to the expected changes near sites of mutation, W265G/M287V produced changes to distant regions suggesting an impact on the overall fold.

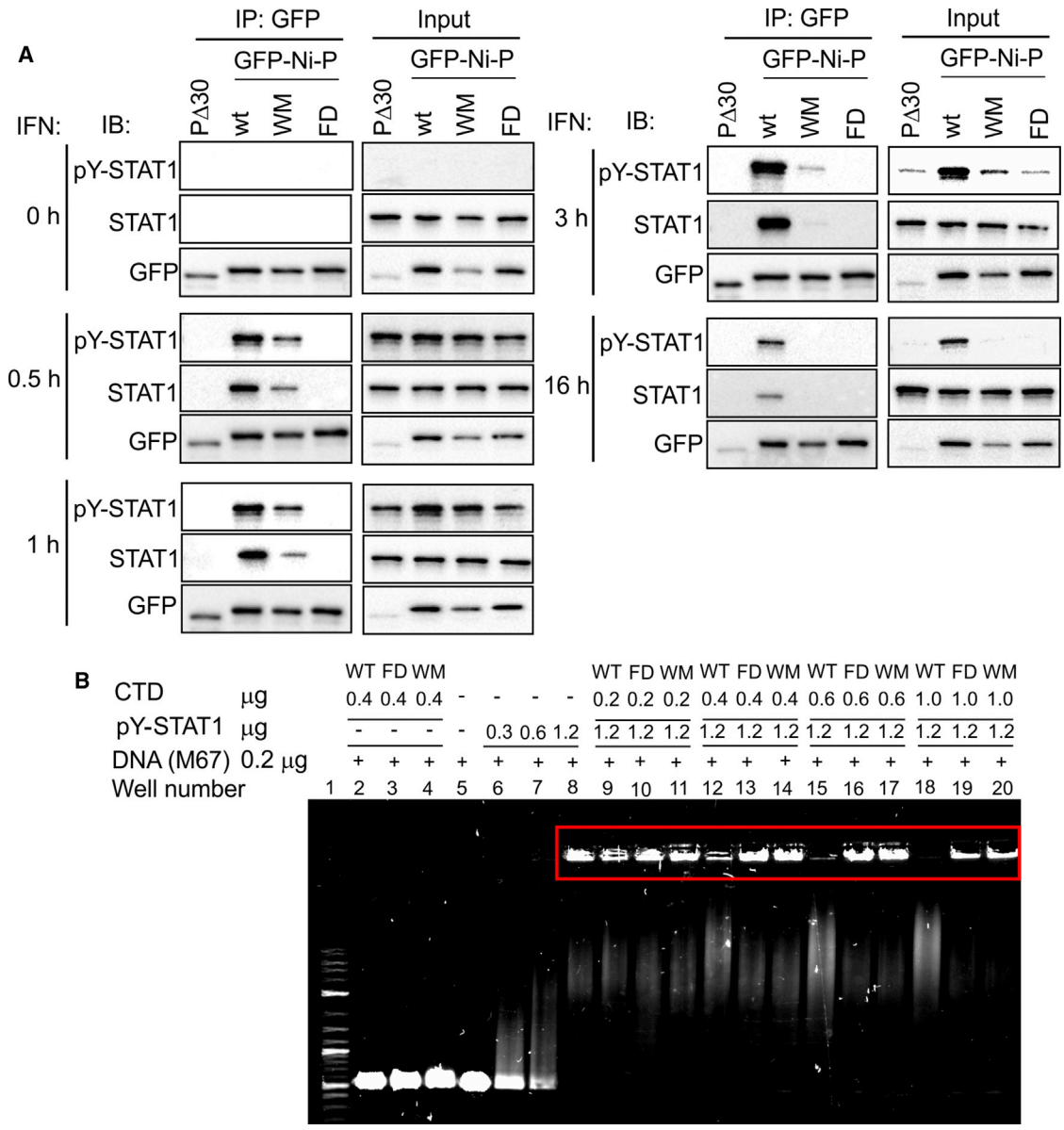

Figure 3. F209A/D235A P-protein Is Deficient for Binding to Activated STAT1 and Disrupting STAT1-DNA Binding

(A) Immunoblot analysis using the indicated antibodies (IBs) of lysate and coIP samples from cells expressing GFP-Ni-P (WT; FD, F209A/D235A; WM, W265G/M287V) or CVS-PΔ30 following IFNα treatment for the indicated times.

(B) A DNA fragment containing GAS sequences was incubated without (well 5) or with WT, FD, or WM P-CTD (wells 2–4) or with phosphorylated (pY) STAT1 pre-incubated without (wells 6–8) or with (wells 9–20) the indicated P-CTD before gel electrophoresis. Protein amounts indicated above gel; lane 1, 2-log DNA ladder; arrest of the DNA fragment within wells is highlighted by red box.

To assess protein stability, we conducted hydrogen-deuterium exchange experiments. Within the time course of the experiment, we determined the exchange rates for a number of amide protons of WT P-CTD (Table S1). In general, F209A/D235A shows faster exchange for all amides compared with WT. For well-resolved resonances for which exchange rates for both WT and F209A/D235A could be determined, differences in free energy for unfolding ($\delta\Delta G$) were estimated to be 4.5–11.3 kJ·mol^{-1} (Table S1). Remarkably, for W265G/M287V, complete hydrogen-deuterium exchange had occurred by the first time point (~20 min), suggesting global destabilization.

We also performed thermal unfolding monitored by CD. The full CD spectra and estimated secondary structure of P-CTD are similar for WT and F209A/D235A (Figure S6A). Although secondary structure content and the shape of the spectra of W265G/M287V were similar to WT and F209A/D235A, the minima were distinctly different. Unfolding of P-CTD shows the WT and F209A/D235A fit to a two-site

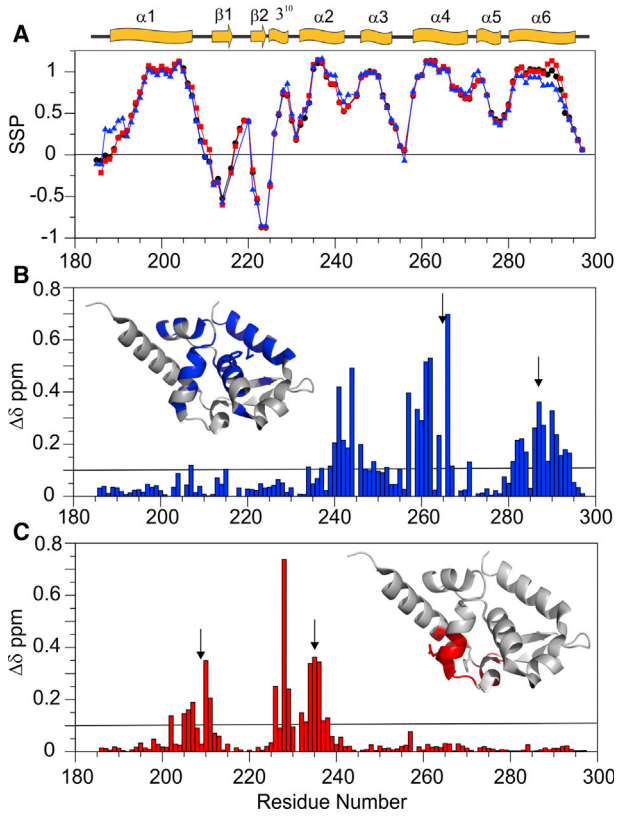

Figure 4. F209A/D235A Causes Minimal Structural Changes to P-CTD

(A) Secondary structure assessment of WT (black), F209A/D235A (red), and W265G/M287V (blue) P-CTD. Positive and negative deviations indicate α-helix and β strand, respectively. Expected secondary structure (on the basis of CVS P-CTD; PDB: 1VYI) shown above.

(B and C) Average chemical shift differences (^{1}H,^{15}N) between WT and W265G/M287V (B) or F209A/D235A (C) P-CTD. Insets show differences >0.1 ppm mapped onto CVS P-CTD. Sites of mutations indicated by arrows; W265G chemical shift difference is 2.4 ppm (not shown) (B).

unfolding model (T_m = 57.0 ± 0.2°C and 51.0 ± 0.7°C, respectively) (Figures S6B and S6C). However, W265G/M287V fits poorly to a two-state model (estimated T_m = 46°C) (Figure S6D).

Collectively, these data indicate that the conformation of W265G/M287V is significantly and globally destabilized compared with WT and F209A/D235A, supporting the idea that W265G/M287V affects STAT1 antagonism via off-target effects, while F209A/D235A disables the interface (region A/B) that binds into the CCD-DBD.

P-CTD Interaction Directly Disrupts STAT1-DNA Binding

The finding that mutations specifically affecting regions A/B prevent P-protein from antagonizing STAT1 transcription suggested that specific contacts with the CCD-DBD, and consequent inhibition of STAT1/DNA interaction, are critical. To examine effects of WT and mutated P-CTD on STAT1/DNA binding in the absence of other cellular factors, we assessed pY-STAT binding to a DNA fragment containing GAS sequences. pY-STAT1 induced a strong concentration-dependent shift in electrophoretic mobility, with most of the DNA becoming arrested in the well at a pY-STAT1:DNA ratio of 1.2:0.2 μg, with only a minor population of lower shifted DNA still apparent within the gel (Figure 3B); WT or mutated P-CTD alone caused no apparent shift of the DNA fragment mobility. Pre-incubation of pY-STAT1 with increasing amounts of WT was clearly inhibitory, preventing arrest of DNA in the well indicative of disruption of the major pY-STAT1/DNA interaction. In contrast, F209A/D235A had little to no impact at any concentration tested, supporting importance of regions A/B in binding to the DBD. W265G/M287V also lacked inhibitory activity, consistent with conformational effects reducing STAT1-binding capacity to a level insufficient to disrupt the interaction. Although WT clearly disrupted the major, strongly shifted pY-STAT1/DNA complex, the lower shifted DNA population remained evident, and appeared more distinct in DNA samples incubated with complexes of WT P-CTD/pY-STAT1 than pY-STAT1 alone or pre-incubated with mutated P-CTD. This is likely indicative of non-specific protein/DNA interactions, possibly through weak electrostatic interactions of the WT P-CTD/pY-STAT1 complex with DNA. Clearly, however, these data indicated that the minimal STAT1-binding region of P-protein, P-CTD, is sufficient to disrupt the major pY-STAT1/DNA interaction. This supports a mechanism whereby formation of discrete P-CTD/STAT1 complexes, not requiring other viral/cellular proteins, antagonizes specific STAT1/DNA interaction, consistent with the direct blockade of the DBD.

F209A/D235A Does Not Interfere with Other Essential P-Protein Functions

Mutagenic studies suggest that the N-RNA binding site of P-protein is a cluster of basic residues (K211, K212, R260) formed by the P-CTD fold (Jacob et al., 2001; Wiltzer et al., 2014). Consistent with distal localization to the W-hole, W-hole mutations did not substantially affect replication (Wiltzer et al., 2014). However, the N-RNA binding site is proximal to region A (Figure 1) and so could be affected by F209A. To assess this, we expressed a peptide (N-peptide) corresponding to a disordered region of N-protein (residues 363–414), which was suggested to mediate P-CTD/N-RNA interaction in a SAXS model (Ribeiro Ede et al., 2009). Two-dimensional ^{15}N,^{1}H HSQC-monitored titrations of ^{15}N-N-peptide with WT and mutant P-CTDs showed significant chemical shift differences in N-peptide (Figure 5A), which fitted to a single-site binding curve (Figure 5B). WT and F209A/D235A showed similar affinities, while W265G/M287V showed >2-fold loss of affinity (Figure 5B). Thus, although W265G/M287V P-CTD clearly retains significant binding to N-protein, permitting normal virus replication (Wiltzer et al., 2014), these data support global structural effects of this mutant. To confirm that N-peptide binding correlates with replication function, we used a minigenome assay in which functional L-protein/P-protein/N-RNA interaction is indicated by luciferase activity (Wiltzer et al., 2014) (Figure 5C). Despite ablation of STAT1 antagonist function, replication function of F209A/D235A P-protein was equivalent to that of WT.

Other than antagonizing IFN signaling, P-protein inhibits IFN induction in infected cells by antagonizing the RIG-I-like receptor pathway (Brzózka et al., 2005; Masatani et al., 2016; Wiltzer et al., 2014). The responsible site(s) in P-protein are not known, but the C-terminal region 152–297 is suggested to be important

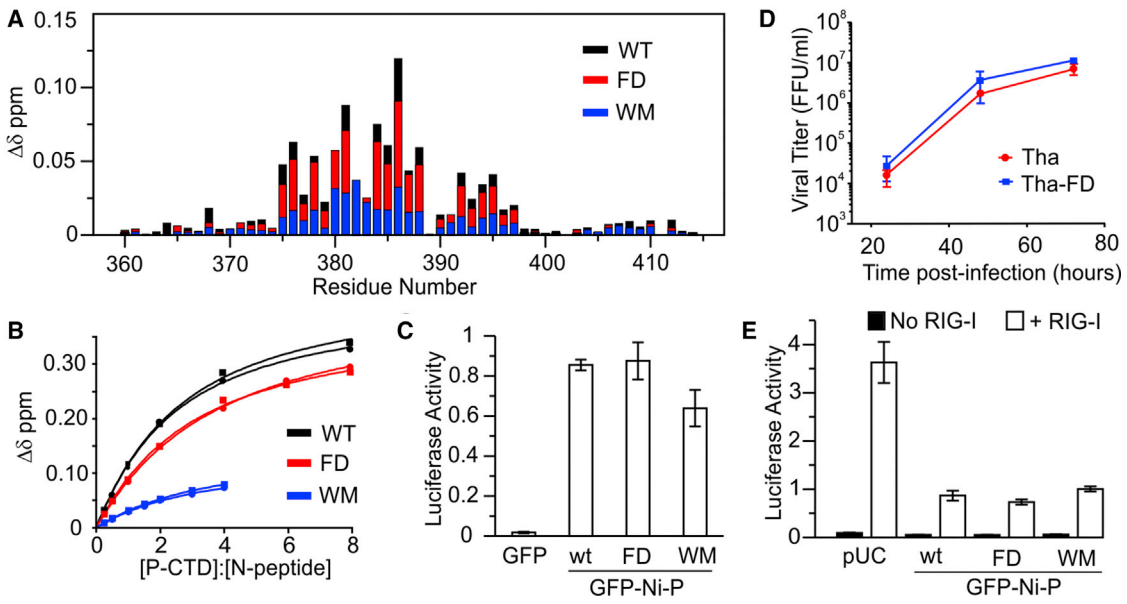

Figure 5. F209A/D235A Does Not Affect Replication or Antagonism of IFN Induction

(A and B) Titration of ^{15}N-labeled N-peptide with WT (black), FD (red), and WM (blue).

(A) Chemical shift difference at 1:0.5 P-CTD/N-peptide.

(B) Single-site saturation binding curves fitted to the change in average chemical shifts (^{1}H,^{15}N) of G385 (squares) and D388 (circles) (WM titration was limited by poor solubility); K_D = 88 ± 4 μM (WT), K_D = 122 ± 11 μM (FD), and K_D = 249 ± 29 μM (WM).

(C) Minigenome assay of GFP-WT, FD, WM Ni-P, or GFP-alone (mean normalized luciferase activity ± SD, n = 3 biological replicates).

(D) Titration of virus in supernatant from BSR cells infected with Tha-WT or Tha-FD (mean ± SD, n = 2 biological replicates).

(E) IFN induction assay of cells transfected to express the indicated GFP-P-protein with or without RIG-I-flag (mean normalized luciferase activity ± SD, n = 3 biological replicates).

Western analyses of lysates used in luciferase assays in (C) and (E) are in Figures S4B and S4C.

(Masatani et al., 2016; Rieder et al., 2011). To determine whether F209A/D235A affects this function, we assessed RIG-I signaling using a reporter assay (Audsley et al., 2016), finding no effect of F209A/D235A or W265G/M287V (the latter consistent with data for CVS-P (Wiltzer et al., 2014)) (Figure 5E). Thus, the new mutations specifically affect the STAT1 targeting arm of P-protein IFN antagonism.

F209A/D235A Mutation Attenuates Street Strain RABV

To assess the role of the STAT1-binding surfaces in infection, we used a recombinant RABV based on the Tha street strain (Thongcharoen et al., 1990). To confirm the potency of mutations in inhibiting STAT1 interaction by Ni- and Tha P-protein (Tha-P), we used a protein-fragment complementation assay (PCA) with a "split" luciferase reporter to measure interactions in cells transfected with WT or mutant P-proteins and STAT1 (Figure 6A). Consistent with the NMR data, normalized luminescence ratio (NLR) values from PCA assays of WT Ni-P/STAT1 interaction in non-IFN-treated cells were comparable with the commonly used threshold of 3.5 for significant interaction (Cassonnet et al., 2011). As NLR values for Ni-P F209A/D235A were clearly reduced (~7-fold), it appears that Ni-P can interact with STAT1 in non-activated cells, dependent on interaction with the CCD-DBD via region A/B. As expected, the NLR for WT Ni-P/STAT1 increased substantially (~3-fold) following IFN treatment. In contrast, values for Ni-P F209A/D235A did not approach the 3.5 threshold. These data are consistent with our findings that interaction with both U-STAT1 (Figure 1) and pY-STAT1 (Figure 3A) is dependent on these residues of regions A/B forming the interface with the CCD-DBD. Assays using Tha-P were comparable with those for Ni-P, confirming conservation of the contact sites (Figure 6A).

We next generated Tha virus encoding WT (Tha-WT) or F209A/D235A-mutated (Tha-FD) P-protein. Assays of virus production in IFN-incompetent BSR cells indicated no difference between Tha-WT and Tha-FD (Figure 5D), consistent with a lack of effect of mutations on replication (Figure 5C). Infection of STING-37 cells that stably express an IFN-dependent luciferase gene, before treatment without or with IFN (Figure 6B), indicated that Tha-WT strongly inhibits luciferase activity in IFN-treated cells compared with that in mock-infected cells. However, in cells infected by Tha-FD, luciferase activity in untreated and IFN-treated cells was not significantly different to that in IFN-treated mock-infected cells, indicating that Tha-FD cannot prevent STAT1 signaling in response to endogenous IFN induced by infection, or exogenous IFN. Consistent with these data, Tha-FD showed significantly impaired pathogenesis compared with Tha-WT following intramuscular inoculation of mice (Figure 6C). As replication in BSR cells was not impaired for the mutant virus, these data are consistent with reduced pathogenesis due to defective evasion of host immunity.

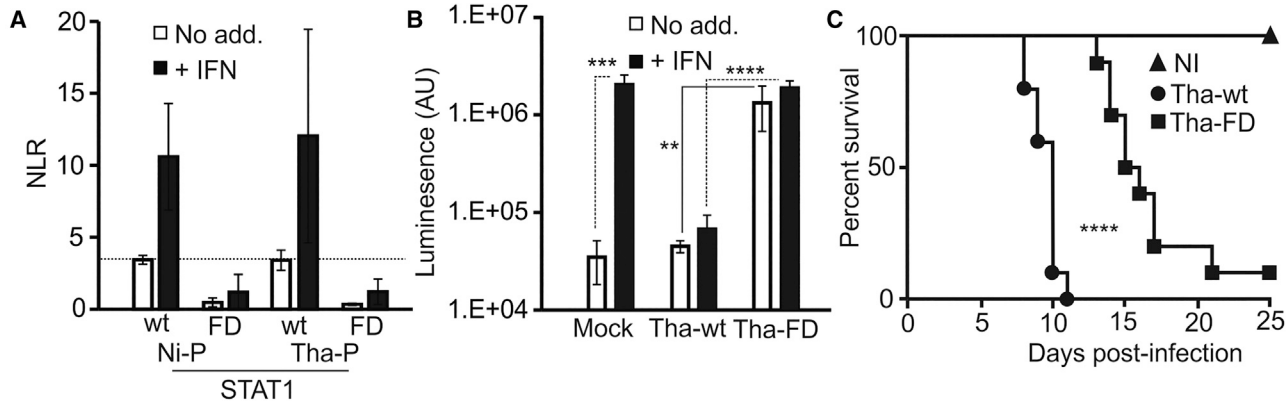

Figure 6. F209A/D235A Impairs STAT1 Targeting by P-Protein and Pathogenicity of a Street Strain RABV

(A) PCA assay of P-proteins and STAT1 fused to luciferase fragments in cells treated without or with IFN (24 h) (mean ± SD, n = 3 biological replicates). Dotted line shows NLR threshold of 3.5.

(B) IFN-dependent luciferase assays of infected STING-37 cells treated without or with IFN (mean AU ± SD, n = 6 biological replicates; **p = 0.0012, ***p = 0.0002, and ****p < 0.0001, Student's t test).

(C) Survival data for infected BALB-c mice. Statistical analysis used log-rank (Mantel-Cox) test, ****p < 0.0001.

Western analyses of lysates of (A) and (B) are in Figures S4D and S4E.

DISCUSSION

Although inhibition of STAT1-mediated IFN signaling is a common mechanism of many pathogenic viruses, the nature of the interaction sites formed between viral proteins and STAT1 remains largely unresolved because of a lack of structural data and consequent reliance on mutagenesis (Nan et al., 2017). To our knowledge, only one crystal structure has been reported for a viral protein with STAT1, comprising a short N-terminal fragment of STAT1 with C-protein of a rodent virus, Sendai virus (Oda et al., 2015). For human pathogens, mass spectrometry hydrogen-deuterium exchange experiments mapped a potential interaction site for truncated STAT1 (residues 1–683) on Ebola virus VP24 (Zhang et al., 2012). However, VP24 antagonism of STAT1 is reported to be due to VP24-importin interaction, which prevents importin-dependent STAT1 nuclear import, with roles for the suggested VP24/STAT1 interaction currently not supported by cell-based studies (Xu et al., 2014). Therefore there is a paucity of structural data on the interface of a viral protein with full-length STAT1.

Our NMR data indicated an extended, complex interface in P-CTD containing three regions, two of which (A and B) form direct contacts with STAT1-CCD-DBD, while the distant region C forms distinct interaction involving the N- and/or C-terminal domains. This interface is in contrast to the small W-hole, mutation of which impaired STAT1 binding (Wiltzer et al., 2014), but for which our NMR analysis did not indicate any contact with STAT1. Indeed, our data indicate that W-hole mutations indirectly reduce STAT1 binding through destabilization of the P-CTD. In contrast, our targeted mutagenesis of the interface identified mutations with localized effects that entirely prevent interaction. Our approach highlights the importance of validating results of mutagenic studies by biophysical approaches, particularly for multifunctional proteins such as IFN antagonists of RNA viruses, for which several similar mutagenic analyses have been reported (Ciancanelli et al., 2009; Röthlisberger et al., 2010).

By revealing the molecular basis of the specific interaction of the P-CTD with the CCD-DBD, our findings highlight the importance of this interface for STAT1 targeting and inhibition of its transcriptional function. Regions A and B, which bind the CCD-DBD, are proximally located on P-CTD but appear to form an extended interface, with each region likely to form distinct interactions with the CCD-DBD, as (1) region A is localized to the round face of the P-CTD, while region B is on the edge of the round and flat faces; (2) the side chains of the surface residues of the respective regions orient in opposite directions, suggesting contacts involve multiple, distinct sites in STAT1; and (3) ablation of STAT1 antagonism requires mutations that affect both regions. Furthermore, we showed that P-CTD alone, dependent on regions A/B, interferes directly with pY-STAT1/DNA interaction in a cell-free assay. Together with previous findings from yeast-two-hybrid and mammalian cell-based assays, this indicates that specific targeting of the CCD-DBD by regions A/B is a major mechanism in immune evasion. Importantly, residues constituting each region of the new interface are conserved among lyssaviruses (Figure S3), suggesting a common mechanism for STAT1 antagonism; furthermore, results from our NMR and mammalian cell-based analyses are consistent with the interface, including the critical binding to the CCD-DBD, being common to U-STAT1 and pY-STAT1. As residues of regions A and B point in opposite directions, it is possible that the IFN-dependent increase in binding to pY-STAT1 in coIPs results from the formation of different dimers by U-STAT1 and pY-STAT1. Specifically, while the binding sites are present in U-STAT1 and pY-STAT1, and can interact with P-CTD, formation of parallel dimers by pY-STAT1 may orient the sites to form simultaneous interactions with P-CTD via opposing monomers contacting regions A and B. Alternatively, pY-STAT1 might form more extensive interaction surfaces increasing affinity.

Delineation of these hypotheses forms the basis of ongoing research.

We previously showed that W265G/M287V renders laboratory RABV strains non-lethal after intracerebral inoculation, validating their potential to contribute to attenuation strategies to improve safety of live vaccines. However, the impact of mutations preventing STAT1 interaction has not been examined in street strains. Clearly, F209A/D235A prevented STAT1 interaction by Tha P-protein and STAT1 antagonism by Tha virus. These data demonstrate critical roles for P-protein/STAT1-CCD-DBD interaction in the immune evasion armory of street strain virus. Importantly, the mutation significantly attenuated pathogenicity of the street strain, indicating key roles in disease caused by high-pathogenicity virus. Nevertheless, the mutated virus retained residual pathogenicity; indeed this mutation does not impair antagonism of IFN induction (Figure 5E), which was reported to be more potent in street compared with fixed RABV strains (Masatani et al., 2016). In addition, M-protein of street strains, but not fixed strains, affects NF-κB signaling, providing additional mechanisms to suppress IFN/cytokine responses (Besson et al., 2017; Luco et al., 2012). The data, however, indicate that these substitutions provide new, minimally disruptive attenuating mutations, which could be used in combination with other mutations to improve the safety of vaccine strains.

Despite the proximity of the STAT1 and N-RNA binding sites in P-CTD (Chenik et al., 1994; Fu et al., 1994), it appears that mutations can be introduced that specifically affect the former without detriment to the latter. Clearly, F209A/D235A produced very specific effects on STAT1 interaction and antagonism, with little to no effect on the affinity or function of N-protein interaction, demonstrating that STAT1 binding and virus replication are spatially distinct. Nevertheless, the proximity of region A of the STAT1-binding site and the predicted N-binding site suggest that binding to these proteins is tightly coordinated by P-protein, with the intriguing possibility that this results in regulation through steric or other mechanisms. Such a mechanism could provide the means for RABV, which has only five protein-encoding genes, to mediate efficient, dynamic coordination of immune evasion and replication during infection. In light of our findings, there is a clear need to extend understanding of P-/N-protein interaction beyond current mutagenic data and the ensuing SAXS models to define how such viruses regulate these functions. The molecular tools and approaches described in the present study should facilitate such research. Furthermore, our approach also has potential application for elucidation of other interactions of the multifunctional P-CTD, including with microtubules (Brice et al., 2016; Moseley et al., 2009), nucleolin (Oksayan et al., 2015), and importins/exportins (Rowe et al., 2016). The methods developed to express, purify, and analyze the functions and interactions of full-length STAT1 should also provide tools for similar analyses of other viral antagonists or cellular regulators.

STAR★METHODS

Detailed methods are provided in the online version of this paper and include the following:

SUPPLEMENTAL INFORMATION

Supplemental Information can be found online at https://doi.org/10.1016/j.celrep.2019.10.020.

ACKNOWLEDGMENTS

We thank Cassandra David for assistance with tissue culture, the Monash Micro Imaging facility (Monash University), and the nuclear magnetic resonance facility (University of Melbourne; Australian Research Council equipment grant LE120100022). This work was supported by National Health and Medical Research Council grant 1125704 to G.W.M., P.R.G., and H.B. and grants 1160838, 1079211, and 1003244 to G.W.M., and Australian Research Council grant DP150102569 to G.W.M.; a Grimwade Fellowship provided by the Meigunyah Fund to G.W.M.; and Japanese Society for the Promotion of Science fellowships S11102 and L14563 to G.W.M.

AUTHOR CONTRIBUTIONS

Conceptualization, P.R.G., G.W.M., N.I., T.O., and H.B.; Methodology, P.R.G., G.W.M., and H.B.; Investigation, M.A.H., A.S., J.Z., P.R.G., Y.-F.M., M.D.W., M.A., S.M.R., K.G.L., G.W.M., F.L., and H.B.; Writing—Original Draft, M.A.H., P.R.G., G.W.M., and H.B.; Writing—Review & Editing, all authors; Funding Acquisition, P.R.G. and G.W.M.; Resources, P.R.G., G.W.M., N.I., T.O., and H.B.

DECLARATION OF INTERESTS

P.R.G., G.W.M., and M.A.H. hold an Australian provisional patent (No. 201901137, "Novel Viruses," 2019).

Received: November 30, 2018
Revised: July 16, 2019
Accepted: October 3, 2019
Published: November 12, 2019

REFERENCES

Audsley, M.D., and Moseley, G.W. (2013). Paramyxovirus evasion of innate immunity: Diverse strategies for common targets. World J. Virol. 2, 57–70.

Audsley, M.D., Marsh, G.A., Lieu, K.G., Tachedjian, M., Joubert, D.A., Wang, L.F., Jans, D.A., and Moseley, G.W. (2016). The immune evasion function of J and Beilong virus V proteins is distinct from that of other paramyxoviruses, consistent with their inclusion in the proposed genus Jeilongvirus. J. Gen. Virol. *97*, 581–592.

Ayed, A., Mulder, F.A., Yi, G.S., Lu, Y., Kay, L.E., and Arrowsmith, C.H. (2001). Latent and active p53 are identical in conformation. Nat. Struct. Biol. *8*, 756–760.

Ben Khalifa, Y., Luco, S., Besson, B., Sonthonnax, F., Archambaud, M., Grimes, J.M., Larrous, F., and Bourhy, H. (2016). The matrix protein of rabies virus binds to RelAp43 to modulate NF-κB-dependent gene expression related to innate immunity. Sci. Rep. *6*, 39420.

Besson, B., Sonthonnax, F., Duchateau, M., Ben Khalifa, Y., Larrous, F., Eun, H., Hourdel, V., Matondo, M., Chamot-Rooke, J., Grailhe, R., and Bourhy, H. (2017). Regulation of NF-κB by the p105-ABIN2-TPL2 complex and RelAp43 during rabies virus infection. PLoS Pathog. *13*, e1006697.

Brice, A., and Moseley, G.W. (2013). Viral interactions with microtubules: orchestrators of host cell biology? Future Virol. *8*, 229–243.

Brice, A., Whelan, D.R., Ito, N., Shimizu, K., Wiltzer-Bach, L., Lo, C.Y., Blondel, D., Jans, D.A., Bell, T.D., and Moseley, G.W. (2016). Quantitative analysis of the microtubule interaction of rabies virus P3 protein: roles in immune evasion and pathogenesis. Sci. Rep. *6*, 33493.

Brunel, J., Chopy, D., Dosnon, M., Bloyet, L.M., Devaux, P., Urzua, E., Cattaneo, R., Longhi, S., and Gerlier, D. (2014). Sequence of events in measles virus replication: role of phosphoprotein-nucleocapsid interactions. J. Virol. *88*, 10851–10863.

Brzózka, K., Finke, S., and Conzelmann, K.K. (2005). Identification of the rabies virus alpha/beta interferon antagonist: phosphoprotein P interferes with phosphorylation of interferon regulatory factor 3. J. Virol. *79*, 7673–7681.

Brzózka, K., Finke, S., and Conzelmann, K.K. (2006). Inhibition of interferon signaling by rabies virus phosphoprotein P: activation-dependent binding of STAT1 and STAT2. J. Virol. *80*, 2675–2683.

Buchholz, U.J., Finke, S., and Conzelmann, K.K. (1999). Generation of bovine respiratory syncytial virus (BRSV) from cDNA: BRSV NS2 is not essential for virus replication in tissue culture, and the human RSV leader region acts as a functional BRSV genome promoter. J. Virol. *73*, 251–259.

Cassonnet, P., Rolloy, C., Neveu, G., Vidalain, P.O., Chantier, T., Pellet, J., Jones, L., Muller, M., Demeret, C., Gaud, G., et al. (2011). Benchmarking a luciferase complementation assay for detecting protein complexes. Nat. Methods *8*, 990–992.

Chenik, M., Chebli, K., Gaudin, Y., and Blondel, D. (1994). In vivo interaction of rabies virus phosphoprotein (P) and nucleoprotein (N): existence of two N-binding sites on P protein. J. Gen. Virol. *75*, 2889–2896.

Cheon, H., Holvey-Bates, E.G., Schoggins, J.W., Forster, S., Hertzog, P., Imanaka, N., Rice, C.M., Jackson, M.W., Junk, D.J., and Stark, G.R. (2013). IFNβ-dependent increases in STAT1, STAT2, and IRF9 mediate resistance to viruses and DNA damage. EMBO J. *32*, 2751–2763.

Ciancanelli, M.J., Volchkova, V.A., Shaw, M.L., Volchkov, V.E., and Basler, C.F. (2009). Nipah virus sequesters inactive STAT1 in the nucleus via a P gene-encoded mechanism. J. Virol. *83*, 7828–7841.

Delaglio, F., Grzesiek, S., Vuister, G.W., Zhu, G., Pfeifer, J., and Bax, A. (1995). NMRPipe: a multidimensional spectral processing system based on UNIX pipes. J. Biomol. NMR *6*, 277–293.

Devaux, P., Hudacek, A.W., Hodge, G., Reyes-Del Valle, J., McChesney, M.B., and Cattaneo, R. (2011). A recombinant measles virus unable to antagonize STAT1 function cannot control inflammation and is attenuated in rhesus monkeys. J. Virol. *85*, 348–356.

Fensterl, V., and Sen, G.C. (2009). Interferons and viral infections. Biofactors *35*, 14–20.

Fu, Z.F., Zheng, Y., Wunner, W.H., Koprowski, H., and Dietzschold, B. (1994). Both the N- and the C-terminal domains of the nominal phosphoprotein of rabies virus are involved in binding to the nucleoprotein. Virology *200*, 590–597.

Ghanem, A., Kern, A., and Conzelmann, K.K. (2012). Significantly improved rescue of rabies virus from cDNA plasmids. Eur. J. Cell Biol. *91*, 10–16.

Huth, J.R., Bewley, C.A., Jackson, B.M., Hinnebusch, A.G., Clore, G.M., and Gronenborn, A.M. (1997). Design of an expression system for detecting folded protein domains and mapping macromolecular interactions by NMR. Protein Sci. *6*, 2359–2364.

Hyberts, S.G., Takeuchi, K., and Wagner, G. (2010). Poisson-gap sampling and forward maximum entropy reconstruction for enhancing the resolution and sensitivity of protein NMR data. J. Am. Chem. Soc. *132*, 2145–2147.

Impagliazzo, A., and Ubbink, M. (2004). Mapping of the binding site on pseudoazurin in the transient 152 kDa complex with nitrite reductase. J. Am. Chem. Soc. *126*, 5658–5659.

Ito, N., Moseley, G.W., Blondel, D., Shimizu, K., Rowe, C.L., Ito, Y., Masatani, T., Nakagawa, K., Jans, D.A., and Sugiyama, M. (2010). Role of interferon antagonist activity of rabies virus phosphoprotein in viral pathogenicity. J. Virol. *84*, 6699–6710.

Ito, N., Moseley, G.W., and Sugiyama, M. (2016). The importance of immune evasion in the pathogenesis of rabies virus. J. Vet. Med. Sci. *78*, 1089–1098.

Jacob, Y., Real, E., and Tordo, N. (2001). Functional interaction map of lyssavirus phosphoprotein: identification of the minimal transcription domains. J. Virol. *75*, 9613–9622.

Jenkins, K., Khoo, J.J., Sadler, A., Piganis, R., Wang, D., Borg, N.A., Hjerrild, K., Gould, J., Thomas, B.J., Nagley, P., et al. (2013). Mitochondrially localised MUL1 is a novel modulator of antiviral signaling. Immunol. Cell Biol. *91*, 321–330.

Kazimierczuk, K., and Orekhov, V.Y. (2011). Accelerated NMR spectroscopy by using compressed sensing. Angew. Chem. Int. Ed. Engl. *50*, 5556–5559.

Lee, W., Tonelli, M., and Markley, J.L. (2015). NMRFAM-SPARKY: enhanced software for biomolecular NMR spectroscopy. Bioinformatics *31*, 1325–1327.

Lim, C.P., and Cao, X. (2006). Structure, function, and regulation of STAT proteins. Mol. Biosyst. *2*, 536–550.

Lin, R., Génin, P., Mamane, Y., and Hiscott, J. (2000). Selective DNA binding and association with the CREB binding protein coactivator contribute to differential activation of alpha/beta interferon genes by interferon regulatory factors 3 and 7. Mol. Cell. Biol. *20*, 6342–6353.

Lucas-Hourani, M., Dauzonne, D., Jorda, P., Cousin, G., Lupan, A., Helynck, O., Caignard, G., Janvier, G., André-Leroux, G., Khiar, S., et al. (2013). Inhibition of pyrimidine biosynthesis pathway suppresses viral growth through innate immunity. PLoS Pathog. *9*, e1003678.

Luco, S., Delmas, O., Vidalain, P.O., Tangy, F., Weil, R., and Bourhy, H. (2012). RelAp43, a member of the NF-κB family involved in innate immune response against Lyssavirus infection. PLoS Pathog. *8*, e1003060.

Mao, X., Ren, Z., Parker, G.N., Sondermann, H., Pastorello, M.A., Wang, W., McMurray, J.S., Demeler, B., Darnell, J.E., Jr., and Chen, X. (2005). Structural bases of unphosphorylated STAT1 association and receptor binding. Mol. Cell *17*, 761–771.

Marsh, J.A., Singh, V.K., Jia, Z., and Forman-Kay, J.D. (2006). Sensitivity of secondary structure propensities to sequence differences between alpha- and gamma-synuclein: implications for fibrillation. Protein Sci. *15*, 2795–2804.

Martin, S.R., and Schilstra, M.J. (2008). Circular dichroism and its application to the study of biomolecules. Methods Cell Biol. *84*, 263–293.

Masatani, T., Ozawa, M., Yamada, K., Ito, N., Horie, M., Matsuu, A., Okuya, K., Tsukiyama-Kohara, K., Sugiyama, M., and Nishizono, A. (2016). Contribution of the interaction between the rabies virus P protein and I-kappa B kinase E to the inhibition of type I IFN induction signalling. J. Gen. Virol. *97*, 316–326.

Mavrakis, M., McCarthy, A.A., Roche, S., Blondel, D., and Ruigrok, R.W. (2004). Structure and function of the C-terminal domain of the polymerase cofactor of rabies virus. J. Mol. Biol. *343*, 819–831.

Moseley, G.W., Lahaye, X., Roth, D.M., Oksayan, S., Filmer, R.P., Rowe, C.L., Blondel, D., and Jans, D.A. (2009). Dual modes of rabies P-protein association with microtubules: a novel strategy to suppress the antiviral response. J. Cell Sci. *122*, 3652–3662.

Nakanishi, T., Miyazawa, M., Sakakura, M., Terasawa, H., Takahashi, H., and Shimada, I. (2002). Determination of the interface of a large protein complex by transferred cross-saturation measurements. J. Mol. Biol. *318*, 245–249.

Nan, Y., Wu, C., and Zhang, Y.J. (2017). Interplay between Janus kinase/signal transducer and activator of transcription signaling activated by type I interferons and viral antagonism. Front. Immunol. *8*, 1758.

Nishida, N., Sumikawa, H., Sakakura, M., Shimba, N., Takahashi, H., Terasawa, H., Suzuki, E., and Shimada, I. (2003). Collagen-binding mode of vWF-A3 domain determined by a transferred cross-saturation experiment. Nat. Struct. Biol. *10*, 53–58.

Oda, K., Matoba, Y., Irie, T., Kawabata, R., Fukushi, M., Sugiyama, M., and Sakaguchi, T. (2015). Structural Basis of the Inhibition of STAT1 Activity by Sendai Virus C Protein. J. Virol. *89*, 11487–11499.

Oksayan, S., Nikolic, J., David, C.T., Blondel, D., Jans, D.A., and Moseley, G.W. (2015). Identification of a role for nucleolin in rabies virus infection. J. Virol. *89*, 1939–1943.

Randall, R.E., and Goodbourn, S. (2008). Interferons and viruses: an interplay between induction, signalling, antiviral responses and virus countermeasures. J. Gen. Virol. *89*, 1–47.

Ribeiro Ede, A., Jr., Leyrat, C., Gérard, F.C., Albertini, A.A., Falk, C., Ruigrok, R.W., and Jamin, M. (2009). Binding of rabies virus polymerase cofactor to recombinant circular nucleoprotein-RNA complexes. J. Mol. Biol. *394*, 558–575.

Rieder, M., Brzózka, K., Pfaller, C.K., Cox, J.H., Stitz, L., and Conzelmann, K.K. (2011). Genetic dissection of interferon-antagonistic functions of rabies virus phosphoprotein: inhibition of interferon regulatory factor 3 activation is important for pathogenicity. J. Virol. *85*, 842–852.

Röthlisberger, A., Wiener, D., Schweizer, M., Peterhans, E., Zurbriggen, A., and Plattet, P. (2010). Two domains of the V protein of virulent canine distemper virus selectively inhibit STAT1 and STAT2 nuclear import. J. Virol. *84*, 6328–6343.

Rowe, C.L., Wagstaff, K.M., Oksayan, S., Glover, D.J., Jans, D.A., and Moseley, G.W. (2016). Nuclear trafficking of the rabies virus interferon antagonist P-protein is regulated by an importin-binding nuclear localization sequence in the C-terminal domain. PLoS ONE *11*, e0150477.

Rupprecht, C.E., Fooks, A.R., and Abela-Ridder, B. (2019). Laboratory Techniques in Rabies, 5th ed, *Vol. 2* (World Health Organization).

Schindelin, J., Arganda-Carreras, I., Frise, E., Kaynig, V., Longair, M., Pietzsch, T., Preibisch, S., Rueden, C., Saalfeld, S., Schmid, B., et al. (2012). Fiji: an open-source platform for biological-image analysis. Nat. Methods *9*, 676–682.

Schoehn, G., Iseni, F., Mavrakis, M., Blondel, D., and Ruigrok, R.W. (2001). Structure of recombinant rabies virus nucleoprotein-RNA complex and identification of the phosphoprotein binding site. J. Virol. *75*, 490–498.

Schuck, P. (2003). On the analysis of protein self-association by sedimentation velocity analytical ultracentrifugation. Anal. Biochem. *320*, 104–124.

Scott, D.J., Gunn, N.J., Yong, K.J., Wimmer, V.C., Veldhuis, N.A., Challis, L.M., Haidar, M., Petrou, S., Bathgate, R.A.D., and Griffin, M.D.W. (2018). A novel ultra-stable, monomeric green fluorescent protein for direct volumetric imaging of whole organs using CLARITY. Sci. Rep. *8*, 667.

Sievers, F., Wilm, A., Dineen, D., Gibson, T.J., Karplus, K., Li, W., Lopez, R., McWilliam, H., Remmert, M., Söding, J., et al. (2011). Fast, scalable generation of high-quality protein multiple sequence alignments using Clustal Omega. Mol. Syst. Biol. *7*, 539.

Studier, F.W. (2005). Protein production by auto-induction in high density shaking cultures. Protein Expr. Purif. *41*, 207–234.

Takahashi, H., Nakanishi, T., Kami, K., Arata, Y., and Shimada, I. (2000). A novel NMR method for determining the interfaces of large protein-protein complexes. Nat. Struct. Biol. *7*, 220–223.

Thongcharoen, P., Sureau, P., Wasi, C., Bourhy, H., Chaiprasithikul, P., and Puthavathana, P. (1990). Monoclonal antibody studies of rabies viruses isolated from Thailand. Southeast Asian J. Trop. Med. Public Health *21*, 129–133.

Versteeg, G.A., and García-Sastre, A. (2010). Viral tricks to grid-lock the type I interferon system. Curr. Opin. Microbiol. *13*, 508–516.

Vidy, A., Chelbi-Alix, M., and Blondel, D. (2005). Rabies virus P protein interacts with STAT1 and inhibits interferon signal transduction pathways. J. Virol. *79*, 14411–14420.

Vidy, A., El Bougrini, J., Chelbi-Alix, M.K., and Blondel, D. (2007). The nucleocytoplasmic rabies virus P protein counteracts interferon signaling by inhibiting both nuclear accumulation and DNA binding of STAT1. J. Virol. *81*, 4255–4263.

Walker, S.R., Chaudhury, M., Nelson, E.A., and Frank, D.A. (2010). Microtubule-targeted chemotherapeutic agents inhibit signal transducer and activator of transcription 3 (STAT3) signaling. Mol. Pharmacol. *78*, 903–908.

Wenta, N., Strauss, H., Meyer, S., and Vinkemeier, U. (2008). Tyrosine phosphorylation regulates the partitioning of STAT1 between different dimer conformations. Proc. Natl. Acad. Sci. U S A *105*, 9238–9243.

Whitmore, L., and Wallace, B.A. (2004). DICHROWEB, an online server for protein secondary structure analyses from circular dichroism spectroscopic data. Nucleic Acids Res. *32*, W668–W673.

Whitmore, L., and Wallace, B.A. (2008). Protein secondary structure analyses from circular dichroism spectroscopy: methods and reference databases. Biopolymers *89*, 392–400.

Wiltzer, L., Larrous, F., Oksayan, S., Ito, N., Marsh, G.A., Wang, L.F., Blondel, D., Bourhy, H., Jans, D.A., and Moseley, G.W. (2012). Conservation of a unique mechanism of immune evasion across the Lyssavirus genus. J. Virol. *86*, 10194–10199.

Wiltzer, L., Okada, K., Yamaoka, S., Larrous, F., Kuusisto, H.V., Sugiyama, M., Blondel, D., Bourhy, H., Jans, D.A., Ito, N., and Moseley, G.W. (2014). Interaction of rabies virus P-protein with STAT proteins is critical to lethal rabies disease. J. Infect. Dis. *209*, 1744–1753.

Xu, W., Edwards, M.R., Borek, D.M., Feagins, A.R., Mittal, A., Alinger, J.B., Berry, K.N., Yen, B., Hamilton, J., Brett, T.J., et al. (2014). Ebola virus VP24 targets a unique NLS binding site on karyopherin alpha 5 to selectively compete with nuclear import of phosphorylated STAT1. Cell Host Microbe *16*, 187–200.

Yang, J., and Stark, G.R. (2008). Roles of unphosphorylated STATs in signaling. Cell Res. *18*, 443–451.

Zhan, J., Hossain, M.A., Sethi, A., Ose, T., Moseley, G.W., and Gooley, P.R. (2019). ^{1}H, ^{15}N and ^{13}C resonance assignments of the C-terminal domain of the P protein of the Nishigahara strain of rabies virus. Biomol. NMR Assign. *13*, 5–8.

Zhang, A.P., Bornholdt, Z.A., Liu, T., Abelson, D.M., Lee, D.E., Li, S., Woods, V.L., Jr., and Saphire, E.O. (2012). The ebola virus interferon antagonist VP24 directly binds STAT1 and has a novel, pyramidal fold. PLoS Pathog. *8*, e1002550.

Zhou, P., and Wagner, G. (2010). Overcoming the solubility limit with solubility-enhancement tags: successful applications in biomolecular NMR studies. J. Biomol. NMR *46*, 23–31.

STAR★METHODS

KEY RESOURCES TABLE

REAGENT or RESOURCE	SOURCE	IDENTIFIER
Antibodies		
Rabbit anti-STAT1	Cell Signaling Technology	Cat#14994; RRID: AB_2737027
goat anti-rabbit Alexa Fluor-568 conjugated secondary	Thermo Fisher	Cat#A-11011; RRID: AB_143157
Mouse anti-pY-STAT1	Cell Signaling Technology	Cat#9176; RRID: AB_2240087
mouse anti-STAT1	BD Biosciences	Cat#610185; RRID: AB_397584
mouse anti-GFP	Roche Applied Science	Cat#11814460001; RRID: AB_390913
HRP-conjugated rabbit anti-mouse secondary	Thermo Fisher	Cat#61-6520; RRID: AB_2533933
Mouse Anti-tubulin	Sigma-Aldrich	Cat#T5168; RRID: AB_477579
Mouse Anti-Flag M2-HRP	Sigma-Aldrich	Cat#A8592; RRID: AB_439702
Mouse anti-GLuc	Biolabs	Cat#E8023S; RRID: AB_1929564
Mouse anti-P 49-1	Ben Khalifa et al., 2016	N/A
FITC-conjugated anti-rabies virus nucleocapsid	Biorad	Cat#3572112
Bacterial and Virus Strains		
Escherichia coli Top10	Thermo Fisher	Cat#C404010
Escherichia coli BL21(DE3)	Thermo Fisher	Cat#C600003
Escherichia coli TKB1- competent cells	Agilent	Cat#200134
rabies strain 8743THA	EVAg collection	Ref-SKU: 014V-02106
Chemicals, Peptides, and Recombinant Proteins		
Adenosine 5′Triphosphate disodium salt	Roche	Cat#10519979001; CAS: 51963-61-2
Coelenterazine H	Biosynth	Cat#C-7004; CAS: 50909-86-9
DNA ladder (2-log DNA ladder)	NEB	Cat#N3200S
Dulbecco's minimal essential medium (DMEM) High Glucose	GIBCO	Cat#12100061
D-[^{13}C] glucose	Sigma-Aldrich	Cat#389374; CAS:11087-42-3
D-[^{2}H]-glucose	Cambridge Isotopes	DLM-2062
Foetal Calf Serum (FCS) (Australian origin)	Serana	Cat#FBS-AU-015
Foetal Calf Serum (FCS) (French origin)	ANSES Ploufragan	N/A
Fugene	Promega	Cat#E2311
Glasgow medium	Thermo Fisher	Cat#11710035
GST-fused 3C protease	In-house	N/A
$^{2}H_2O$	Sigma-Aldrich	Cat#151882; CAS:7789-20-0
Interferon: Universal Type 1 – recombinant Human Interferon Alpha (IFNα)	PBL Assay Science	Cat#PBL-11200-2
Lipofectamine 2000	Thermo Fisher	Cat#11668-019
Lipofectamine 3000	Thermo Fisher	Cat#L3000-015
D-luciferin	Sigma	Cat#L9504; CAS:103404-75-7
4-(6 Methyl-1,3-benzothiazol-2-yl)aniline	Novachem	Cat#211723-1g; CAS:92036-4
$^{15}NH_4Cl$	Sigma-Aldrich	Cat#299251; CAS:39466-62-1
OneTaq DNA Polymerase	NEB	Cat#M0482S
Passive 5 x Lysis Buffer	Promega	Cat#E1941
SYBR Safe	Invitrogen	Cat#S33102
Critical Commercial Assays		
Firefly Luciferase kit	Promega	Cat#E1500
Renilla Luciferase kit	Promega	Cat#E2810

(*Continued on next page*)

Continued

REAGENT or RESOURCE	SOURCE	IDENTIFIER
GFP-Trap-MAG system	Chromotek	Cat#gtma-20 GFP-Trap®_MA
Western Lightening ECL PLUS	Perkin Elmer	Cat#NEL105001EA
Change-IT™ Multiple Mutation Site-Directed Mutagenesis Kit	Afflymetrix	Cat#78480
Phusion Site-Directed Mutagenesis Kit	Thermo Fisher	Cat#F541
PrimeSTAR Max DNA Polymerase	Takara	Cat#R045B
Deposited Data		
Biological Magnetic Resonance Bank	Zhan et al., 2019	27498
Experimental Models: Cell Lines		
BSR-T7	Gift from Karl-Klaus Conzelmann (Buchholz et al., 1999)	N/A
COS-7	ATCC	Cat#CRL-1651
HEK293-T (Australian origin)	ATCC	Cat#CRL-3216
HEK293-T (French origin)	ATCC	Cat#CRL-1573
STING-37	Gift from Marianne Lucas-Hourani (Lucas-Hourani et al., 2013)	N/A
Experimental Models: Organisms/Strains		
BALB/C mice	Charles River Laboratory	Cat#24980671-A
Oligonucleotides		
Table S2	N/A	N/A
Recombinant DNA		
pGEV2	Huth et al., 1997	Addgene Cat#12616
pGEV2-STAT1	This paper	N/A
pGEV2-STAT1-CCD-DBD	This paper	N/A
pGEX6P3	GE Healthcare	Cat#28-9546-51
pGEX6P3-N-pep	This paper	N/A
pGEX6P2-STAT1	This paper	N/A
pET28a	Novagen	Cat#69864
pET28a-NiP-CTD	Zhan et al., 2019	N/A
pET28a-NiP-CTD (mutants)	This paper	N/A
pET28a-GFP-NiP-CTD	This paper	N/A
pEGFP-C1	Clontech	Cat#6084-1
pEGFP-C1-Ni-P	Wiltzer et al., 2012	N/A
pEGFP-C1-Ni-P (mutants)	This paper	N/A
pEGFP-C1-PΔ30	Wiltzer et al., 2012	N/A
pCMV-KDEL-Glu1	Brunel et al., 2014	N/A
pCMV-KDEL-Glu2	Brunel et al., 2014	N/A
pRL-TK	Promega	Cat#E2241
pISRE-Luc	Stratagene	Cat#219089
pGL3-IFNβ	gift from Rongtuan Lin (Lin et al., 2000)	N/A
RIG-I-flag	Gift from Ashley Mansel (Jenkins et al., 2013)	N/A
pRVDI-luc	Wiltzer et al., 2014	N/A
pC-RN	Wiltzer et al., 2014	N/A
pC-RL	Wiltzer et al., 2014	N/A
pGL4.50	Promega	
pSDI-Flash-HH-SC	Ghanem et al., 2012	N/A
Tha- wt_pSDI-Flash-HH-SC	Ben Khalifa et al., 2016	N/A

(*Continued on next page*)

Continued

REAGENT or RESOURCE	SOURCE	IDENTIFIER
Tha- FD_pSDI-Flash-HH-SC	This paper	N/A
N-pTIT	Ben Khalifa et al., 2016	N/A
P-pTIT	Ben Khalifa et al., 2016	N/A
L-pTIT	Ghanem et al., 2012	N/A
Tha-P-wt_Flag_Glu2	This paper	N/A
Tha-P-FD_Flag_Glu2	This paper	N/A
Ni-P-wt_Flag_Glu2	This paper	N/A
Ni-P-FD_Flag_Glu2	This paper	N/A
Glu1-HA-Stat1	This paper	N/A
4xM67 pTATA TK-luc	Gift from David Frank (Walker et al., 2010)	N/A
Software and Algorithms		
Image Lab 5.2.1	BioRad	https://www.bio-rad.com
NMRFAM-SPARKY	Lee et al., 2015	https://nmrfam.wisc.edu/nmrfam-sparky-distribution
NMRPipe	Delaglio et al., 1995	https://www.ibbr.umd.edu/nmrpipe
SSP	Marsh et al., 2006	http://abragam.med.utoronto.ca/~JFKlab/
SEDFIT	Schuck, 2003	www.analyticalultracentrifugation.com
Prism version 7	GraphPad	https://www.graphpad.com
qMDD	Kazimierczuk and Orekhov, 2011	mddnmr.spektrino.com
xcrvfit 4.0.12	Boyko and Sykes	www.bionmr.ualberta.ca
FIJI	Schindelin et al., 2012	https://imagej.net/Fiji/Downloads
Clustal Omega	Sievers et al., 2011	https://www.ebi.ac.uk/Tools/msa/clustalo/
Other		
Jupiter 5 μm C18 300 Å, 10 × 250 mm column	Phenomenex	Cat#005-4053-N0
Glutathione Sepharose 4 Fast Flow resin	GE Healthcare	Cat#17513202
HiLoad™ 16/60 Superdex™ 75 prep grade	GE Healthcare	Cat#208-9893-33
HiLoad™ 16/60 Superdex™ 200 prep grade	GE Healthcare	Cat#28-9893-35
Talon® metal-affinity resin	Clontech, Takara	Cat#635504
HiTrap Heparin	GE Healthcare	Cat#17-0406-01

LEAD CONTACT AND MATERIALS AVAILABILITY

Further information and requests for resources and reagents should be directed to and will be fulfilled by the Lead Contact Paul Gooley (prg@unimelb.edu.au). Plasmids and proteins generated in this study will be made available on request following a completed Materials Transfer Agreement. The recombinant strain of rabies virus, Tha-rec, is available via the website of the biobanking EVAg portal (https://www.european-virus-archive.com, ref Ref-SKU: 014V-03194). There are restrictions to the availability of viruses due to biosecurity concerns and international regulations.

EXPERIMENTAL MODEL AND SUBJECT DETAILS

Bacterial cultures

Escherichia coli BL21 (DE3) and *E.coli* TKB1-competent cells were kept at −80°C. These cells were freshly transformed prior to culturing for protein expression as described in Methods Details.

Mammalian cell cultures

HEK293-T (human cell line), COS-7 (african green monkey cell line), BSR (golden hamster cell line) and 'STING-37' cells (HEK293 cells (human cell line) stably transfected with an ISRE-luciferase reporter gene-37; kindly provided by Marianne Lucas-Hourani, Unité de Génomique Virale et Vaccination, Virology Department, Institut Pasteur) (Lucas-Hourani et al., 2013) were cultured at 37°C, 5% CO_2, in Dulbecco's minimal essential medium (DMEM) supplemented with 10% fetal calf serum (FCS). BSR-T7 cells, kindly provided by Karl-Klaus Conzelmann (Max von Pettenkofer Institute and Gene Center, Munich) (Buchholz et al., 1999), were cultured in

Glasgow medium supplemented with 10% FCS, tryptose phosphate, non-essential amino acids and geneticin and were used to rescue the mutated Tha-FD virus.

In vivo experiments

Three-week-old female BALB/C mice were infected by intramuscular injection of 1000 FFUs of recombinant RABV, and monitored for 25 days. 10 mice were infected with each recombinant RABV; 5 mice were tested per virus in each of 2 separate assays. Mice were sacrificed when late infection symptoms appeared (humane endpoint). All mouse experiments were performed in accordance with the European and French guidelines (Directive 86/609/CEE and Decree 87–848 of 19 October 1987) and the Institut Pasteur Safety, Animal Care and Use Committee, and approved by the French Administration (Ministère de l'Enseignement et de la Recherche) under the number O522-02. All animals were handled in strict accordance with good animal practice.

METHOD DETAILS

Design of Constructs

For GB1-STAT1 expression vectors cDNA for full-length STAT1 (4-750) or STAT1-CCD-DBD (136-490) was inserted into pGEV2 vector to generate a GB1-fusion protein with a thrombin-cleavable linker between GB1 and STAT1, and C-terminal His_6-tag. For GST-STAT1, full-length STAT1 was cloned into pGEX-6P-2.

To generate a His_6-tagged protein with TEV cleavage site, P-CTD (186-297) (Nishigahara RABV strain) with the C-terminal cysteine (Cys297) mutated to serine, with or without fusion to cDNA encoding an ultra-stable monomeric GFP (GFP-P-CTD) (Scott et al., 2018) was cloned into the *NdeI-EcoRI* sites of pET28a. To produce N-peptide with an N-terminal GST and PreScission protease cleavage site, cDNA for residues 363-414 of N-protein containing S389E substitution was cloned into pGEX-6P-3 at BamHI-*XhoI* sites. Expression constructs for expression of GFP-fused P-proteins in mammalian cells are described elsewhere (Wiltzer et al., 2012). For PCA assays P-protein or STAT1 sequences were cloned into vectors containing the N-terminal (pCMV-KDEL-Glu1) or C-terminal part (pCMV-KDEL-Glu2) of *Gaussia* luciferase, respectively, using *BstXI/SalI* and *XhoI/SacII* restriction sites (Brunel et al., 2014). Mutagenesis used PrimeSTAR Max DNA Polymerase (Takara) following manufacturer's instructions and confirmed by sequencing. All primers used for these constructs are in Table S2.

Protein expression and purification

GB1-STAT1 constructs were expressed in *E. coli* BL21 (DE3) in 2YT autoinduction media (Studier, 2005) with shaking (16°C, 225-230 rpm). Pellets from 500 mL cultures were resuspended in 50 mL extraction buffer (50 mM Na_2HPO_4, 300 mM NaCl, 10 mM imidazole, pH 7.4 with one Complete-EDTA free Protease Inhibitor tablet), homogenized and lysed (Avestin EmulsiFlex C3 cell crusher). Following centrifugation (13,000 *g*, 30 min, 4°C), supernatant was filtered (0.22 μm), applied to 5 mL Talon^R metal-affinity resin (Clontech, Takara) in a gravity-flow column (binding for 90 min, 4°C). Unbound proteins were discarded by washing (100 mL extraction buffer) and GB1-fusion proteins were eluted (80 mL of 50 mM Na_2HPO_4, 300 mM NaCl, 300 mM imidazole, pH 7.4). Fractions were concentrated to 1.5 mL (Amicon Ultra-15 MWCO 10 kDa (STAT1 truncates) or 30 kDa (full-length STAT1)) subjected to size exclusion chromatography (SEC) on a HiLoad^{TM} 16/60 Superdex^{TM} 200 prep grade column pre-equilibrated with 50 mM Na_2HPO_4, 100 mM NaCl, 1 mM dithiothreitol (DTT), pH 6.8 and run at flow rate of 1 mL/min (Figure S1A). Eluted 1 mL fractions were collected, pooled, and reconcentrated. GST-tagged STAT1 was purified similarly except, after centrifugation, filtered supernatant was bound to 5 mL Glutathione Sepharose 4 Fast Flow resin (GE Healthcare) pre-equilibrated in 50 mM Na_2HPO_4, 300 mM NaCl, 1 mM DTT, pH 7.4. After 90 min, unbound proteins were removed and GST-STAT1 was eluted (80 mL of 50 mM Na_2HPO_4, 300 mM NaCl, 10 mM reduced glutathione, 1 mM DTT, pH 7.4); cleaved overnight using 100 μL purified 96 μM GST-fused 3C protease (4°C); concentrated to 1.5 mL and further purified with SEC as above (Figure S1A).

To produce tyrosine phosphorylated STAT1 (pY-STAT1), GB1-STAT1 pGEV2 construct was transformed into *E.coli* TKB1-competent cells (Agilent technologies) and expressed and purified as described above except that, following 2 h growth post-IPTG, cells were grown for a further 2 h (20°C) in the presence of indole acrylic acid to induce the plasmid encoding Elk tyrosine kinase. Cells were lysed and purified in a similar manner as described above. To separate unphosphorylated STAT1 from pY-STAT1 the protein elution obtained from the metal affinity purification was subjected to a Heparin column (GE healthcare) equilibrated with 20 mM Tris HCl, 1 mM EDTA and 2 mM DTT with no salt (HA-buffer) before elution with 25 mL of HA-buffer with 150 mM KCl (to remove un-phosphorylated STAT1) and 25 mL of HA-buffer with 400 mM KCl to elute pY-STAT1. pY-STAT1 was further purified by SEC using a Superose 6 10/300 increase column (GE healthcare) with a flow rate of 1 mL/min.

Unlabelled P-CTD or GFP-P-CTD (WT or mutant) proteins were expressed similarly to GB1-STAT1 except that ^{15}N-labeled P-CTD was expressed in an autoinduction media using $^{15}NH_4Cl$ as a sole nitrogen source (Studier, 2005). For labeling with ^{13}C and ^{15}N isotopes, cells were grown in N-5052 (Studier, 2005) supplemented with 1 g/L of $^{15}NH_4Cl$ (Sigma-Aldrich), 3 g/L of D-[^{13}C] glucose (Sigma-Aldrich) as sole sources of nitrogen and carbon (Zhan et al., 2019). Cells were grown at 37°C to OD_{600} 0.6-0.7, transferred to 16°C and induced (0.4 mM IPTG with shaking overnight, 225-230 rpm). To express ^2H,^{15}N-labeled P-CTD, cells were grown in N-5052 medium with 1 g/L of $^{15}NH_4Cl$ and 2 g/L of D-[^2H]-glucose (Cambridge Isotope Laboratories) in ^2H_2O (Sigma-Aldrich). A 5 mL pre-culture prepared from a single colony incubated at 37°C for 6-7 h was centrifuged, washed, and resuspended into N-5052 media prepared in ^2H_2O and with $^1H_6$-glucose as the carbon source for overnight culture. Cells adapted to the deuterated

media were pelleted, washed, and diluted in N-5052 media supplemented with D-[^{2}H]-glucose. After adapting to 16°C, cells were induced (0.4 mM IPTG) at OD600 0.7∼0.8 and expressed overnight. P-CTD proteins were purified over Talon® metal-affinity resin, cleaved with TEV protease (0.5 mL of 1.8/mg/mL of purified TEV to 50 mL of protein sample) in the presence of 1 mM DTT. After cleavage the protein was concentrated to 1.5 mL, and subjected to SEC (HiLoad™ 16/60 Superdex™ 75 prep grade column for P-CTD; HiLoad™ 16/60 Superdex™ 200 prep grade column for GFP-P-CTD) with a flow rate of 1 mL/min.

To assess effects of P-CTD mutations on solubility of expressed protein, similar volumes of bacterial expression cultures were lysed and fractionated into soluble supernatant and insoluble debris, and separated by SDS-PAGE. Solubility index was calculated using the band intensities using Image Lab 5.2.1 (Biorad).

^{15}N-labeling of N-peptide was conducted similarly to P-CTD, except that extraction buffer for processing of cell pellets was 50 mM Na_2HPO_4, 300 mM NaCl, 1 mM DTT at pH 7.5, and, following cell crushing and centrifugation, clear supernatant was bound to 5 mL of Glutathione Sepharose 4 Fast Flow resin packed into a gravity-flow column (4°C, 2 h). Unbound material was removed by washing (100 mL extraction buffer) and on-column cleavage used 3C protease (above) for 4 h at 4°C. Cleaved peptide was eluted by gravity flow (20 mL of extraction buffer). After concentrating to 5 mL using Amicon Ultra-15 (MWCO 3 kDa) peptide was further purified by reverse-phase high performance liquid chromatography using a 0 to 60% acetonitrile gradient (0.1% trifluoracetic acid) applied over 60 min at a flow rate of 5 mL/min using a C18 column (Phenomenex Jupiter 5 μm C18 300, 10 × 250 mm) Collected fractions were pooled, freeze-dried and stored at −20°C. The final yield obtained was 3-5 mg/L of bacterial culture.

Circular Dichroism spectrophotometry

CD spectrophotometry used a 410 SF CD spectrometer (AVIV Biomedical, Lakewood, NJ). Measurements used a quartz cuvette (0.1 cm path length) and 0.1-0.2 mg/mL protein in 50 mM Na_2HPO_4, 100 mM NaCl, 1mM DTT, pH 6.8 at 25°C (Figures S1C and S6A). A wavelength range of 190-260 nm was scanned with an increment of 0.5 nm and averaging time of 1.0 s. For each protein three scans were recorded, averaged, and subtracted from three averaged buffer scans. Mean residue ellipticity (MRE) (deg.cm^2.dmol^{-1}) was calculated using MRE = θ.MRW/10.l.c, where θ is the ellipticity (millidegrees), l is the pathlength (cm), c is the protein concentration (mg/mL) and MRW is the Mean Residue Weight calculated as MRW = Mr/(N-1), where Mr is the MW of the protein (Da) and N is number of residues. Secondary structure analysis was conducted in DichroWeb (Whitmore and Wallace, 2004, 2008) using the program CDSSTR.

Thermal unfolding was measured by raising sample temperature from 20 to 90°C at a rate of 1°C/min (Figures S6B–S6D). Thermal unfolding transitions and mid-point melting temperature (T_m) were calculated by plotting normalized ellipticity values at 222 nm as a function of temperature and fitted to a two-state transition (Equation 1), assuming no change to heat capacity for folded and unfolded, and correcting for pre- and post-transition changes (Martin and Schilstra, 2008):

$$Y = \frac{(Y_N + \beta_N T) + (Y_D + \beta_D T)e^{-\left(\Delta H_{Tm}\left(1-\left(\frac{T}{Tm}\right)\right)/RT\right.}}{1 + e^{-\left(\Delta H_{Tm}\left(1-\left(\frac{T}{Tm}\right)\right)/RT\right.}} \quad (1)$$

where Y is the observed ellipticity at a given temperature, Y_N (Y_D) and β_N (β_D) are the slopes and intercepts of the pre- and post-transition slopes; T is temperature (°C), T_m the mid-point melting temperature, and ΔH_{Tm} is the enthalpy at T_m.

Analytical ultracentrifugation

Sedimentation Velocity Analytical Ultracentrifuge (SV-AUC) experiments were conducted on a Beckman Optima XL-I AUC equipped with an An50 Ti rotor (Beckman Coulter, IN). Protein samples were dialysed against 50 mM Na_2HPO_4, 100 mM NaCl, 2 mM TCEP, pH 6.8 (SV-AUC buffer). Samples containing GB1-STAT1 proteins at varying molarities were loaded into the sample compartments of Epon double-sector centerpieces, with SV-AUC buffer in the reference compartment. Samples were centrifuged at 50,000 rpm (20°C), and monitored continuously at 280 nm. Fluorescence-detected SV-AUC (FDS-AUC) experiments used a Beckman Optima XL-A AUC equipped with a fluorescence-detection system (AVIV Biomedical, Lakewood, NJ). GFP-P-CTD concentration was kept constant (10 μM); GB1-STAT1 (5 to 20 μM) and GB1-CCD-DBD (5 to 40 μM) were diluted in SV-AUC buffer. Samples were centrifuged at 50,000 rpm (20°C) and monitored continuously. Data were fitted in SEDFIT (Schuck, 2003) using 100 sedimentation coefficient increments from 0 to 15 S, with regularization parameter of p = 0.95. Frictional ratios were fitted, and for the fluorescence-detected experiments, meniscus positions were fitted.

Nuclear Magnetic Resonance spectroscopy

P-CTD and STAT1 samples were dialyzed in 50 mM Na_2HPO_4, 100 mM NaCl, and 1 mM DTT, pH 6.8 (NMR buffer) prior to making final samples in 10% D_2O/90% H_2O. NMR data were acquired at 25°C on a Bruker Avance IIIHD 700 MHz spectrometer equipped with a triple resonance cryoprobe. The near-complete assignment of the ^{1}H,^{13}C,^{15}N resonances of WT P-CTD are reported elsewhere (Zhan et al., 2019) (Biological Magnetic Resonance Bank, accession code 27498). To assign backbone (HN, ^{15}N, ^{13}Cα, ^{13}Cβ, ^{13}C') resonances of P-CTD mutants, data were collected for the 3D experiments (HNCO, HN(CA)CO, HNCACB, HNCOCACB) using uniformly ^{13}C-^{15}N labeled protein. 2D ^{15}N,^{1}H Heteronuclear Single Quantum Coherence (^{15}N,^{1}H HSQC) spectra were collected using traditional approaches whereas 3D spectra were recorded using 10% non-uniform sampling (NUS) and Poisson gap sampler

(Hyberts et al., 2010). Spectra were reconstructed with the compressed sensing algorithm using qMDD (Kazimierczuk and Orekhov, 2011), processed using NMRPipe (Delaglio et al., 1995), and analyzed with NMRFAM-SPARKY (Lee et al., 2015). Secondary structure of the P-CTD mutants was assessed using SSP with $^{13}C\alpha$ and $^{13}C\beta$ chemical shift data (Marsh et al., 2006).

Interactions between 30 μM ^{15}N-labeled P-CTDs and GB1-STAT1 were monitored by acquiring ^{15}N,^{1}H HSQC spectra with and without 30 μM GB1-STAT1. For transferred cross-saturation experiments (Impagliazzo and Ubbink, 2004; Nakanishi et al., 2002; Nishida et al., 2003) 500 μM uniformly labeled ^{2}H,^{15}N P-CTD was mixed with 50 μM GB1-STAT1 protein in NMR buffer in 90% $^{2}H_2O$/10% H_2O. Prior to mixing, ^{2}H,^{15}N P-CTD was kept in the same buffer for 8 h at room temperature and then 2 days at 4°C to allow amide exchange to reach equilibrium. The transferred cross-saturation experiments used a 2D ^{15}N, ^{1}H TROSY-HSQC pulse scheme and WURST ^{1}H-saturation pulse (15 ms, 2800 Hz band-width) (Takahashi et al., 2000). Data were acquired with 25% NUS with interleaved rows for on- and off-resonance saturation; spectral widths of 12 ppm in ^{1}H (2048 data points), and 27 ppm in ^{15}N (512 data points). The WURST saturation of the aliphatic protons of P-CTD was 2 s with a saturation frequency set at 0.9 ppm for on-resonance and −50 ppm for off-resonance. Each transferred cross-saturation experiment was acquired in 6 to 13 h with 64 to 112 scans per row and a recycle time between scans of 1 s. Spectra were reconstructed with the compressed sensing algorithm using qMDD (Kazimierczuk and Orekhov, 2011) and processed using NMRPipe (Delaglio et al., 1995).

To monitor the binding of N-peptide to P-CTD, 2D ^{15}N,^{1}H HSQC-monitored titrations were conducted using 50 μM of ^{15}N-labeled N-peptide with an increasing concentration (25 to 500 μM) of unlabelled P-CTD variants. During the titration, the volume of the NMR sample was kept within a variation of 10%. The average chemical change was determined from (Ayed et al., 2001):

$$\Delta\delta\ ppm = \left(\left(\Delta^{1}HN\right)^{2} + \left(0.15\Delta^{15}N\right)^{2}\right)^{1/2} \quad (2)$$

Dissociation constants (K_D) were measured using well-resolved peaks that showed the largest shifts and remained in fast exchange during the titration. Data were fitted to a non-linear curve assuming a two-state exchange (xcrvfit 4.0.12; Boyko and Sykes, University of Alberta, www.bionmr.ualberta.ca).

Hydrogen-deuterium exchange was monitored via acquisition of 2D ^{15}N, ^{1}H HSQC spectra (25°C, pH 6.8) on a 600 MHz Bruker Avance III spectrometer. Exchange was initiated by passing a 250 μM sample over an Illustra NAP-5 column pre-equilibrated in NMR buffer, 100% D_2O. Data were acquired with spectral widths of 13 ppm in ^{1}H (2048 data points) and 26 ppm in ^{15}N (256 data points). NUS was used for acquisition with 25% sampling. For each spectrum 16 scans were acquired per ^{15}N data point resulting in acquisition times of 20 min. Acquisition of the first spectrum occurred after 8 mins following initial exchange. Exchange rates (k_a) (Table S1) were determined by fitting to a single exponential,

$$I = e^{-k_a t} \quad (3)$$

where I is the peak intensity, k_a the exchange rate and t is time. The difference in free energy of exchange (δΔG kJ/mol) between WT and mutant protein was determined from

$$\delta\Delta G = -RTln\left(\frac{k_{a1}}{k_{a2}}\right) \quad (4)$$

where R is the gas constant, T is temperature (K) and k_{a1} and k_{a2} are the exchange rates for the same proton of WT and mutant protein.

Multiple sequence alignment

Clustal Omega (Sievers et al., 2011) was used with default settings for the multiple sequence alignment of the lyssavirus P proteins in Figure S3.

Luciferase reporter gene assays

For dual luciferase assays for type I IFN signaling or induction of type I IFN (Audsley et al., 2016), HEK293-T cells cultured in wells of a 24-well plate were co-transfected with pEGFP-C1 constructs encoding GFP-fused WT or mutant P-protein, pRL-TK (Promega) (which constitutively expresses *Renilla* luciferase) and either pISRE-Luc (Stratagene, for type I IFN signaling assays) or pGL3-IFNβ (kindly provided by Rongtuan Lin, McGill University, Quebec, Canada, for induction assays) (Lin et al., 2000); pISRE-Luc and pGL3-IFNβ express firefly luciferase under the control of an ISRE promoter or IFNβ promoter respectively. Transfection used Fugene (Promega) or Lipofectamine 2000 (ThermoFisher), according to the manufacturer's instructions. For IFN induction assays, co-transfection included RIG-I-flag (to activate RIG-I signaling (Jenkins et al., 2013; Wiltzer et al., 2014)) and/or pUC18 to equalise total DNA transfected for samples without transfection of RIG-I or P-protein constructs. 24 h post-transfection, cells were lysed using passive lysis buffer (Promega) and luciferase activity measured by dual luciferase assay as previously (Audsley et al., 2016; Wiltzer et al., 2012, 2014) in 96-well plates using a BMG CLARIOstar plate-reader with solution A for firefly luminescence (200 mM Tris–HCl, 15 mM $MgSO_4$, 0.1 mM EDTA, 25 mM DTT, 1 mM ATP, 200 μM luciferin, pH 8.0) and solution B for *Renilla* luminescence (25 mM Na_4PPi, 10 mM NaAc, 15 mM EDTA, 500 mM Na_2SO_4, 500 mM NaCl, 50 μM 4-(6-Methyl-1,3-benzothiazol-2-yl)aniline, 4 μM benzyl-coelenterazine, pH 5.0). For assays of IFN signaling, cells were treated 7 h post-transfection with 1000 U/mL IFNα (PBL Interferon Source) for 16 h before analysis by dual luciferase assay (Wiltzer et al., 2012). Values for firefly luciferase activity were then

normalized to those for *Renilla* luciferase activity by calculating the ratio of firefly luminescence to *Renilla* luminescence (Audsley et al., 2016).

For minigenome assays (Wiltzer et al., 2014) HEK293-T cells cultured in 12-well dishes were transfected with 0.4 μg pRVDI-luc, 0.6 μg pC-RN, 0.2 μg pC-RL, 0.025 μg pRL-TK, and 0.1 μg pEGFP-C1 encoding GFP-fused WT or mutant P-protein, using Lipofectamine 2000. 48 h later cells were lysed in passive lysis buffer and luciferase activity was measured 48 h later by dual luciferase assay and normalized as described above.

IFN signaling in infected cells was measured using STING-37 cells (Lucas-Hourani et al., 2013) plated at 1×10^6 cells/mL in 96-well plates in 100 μL of medium. Cells were infected at a multiplicity of infection (MOI) of 1 FFU/cell, or mock infected, then treated 24 h later without or with 1000 U/mL IFNα, before analysis using the Firefly Luciferase kit (Promega, France) after 24 h incubation.

Confocal laser scanning microscopy (CLSM)

COS-7 cells growing on coverslips were transfected with pEGFP-C1 plasmids expressing WT or mutant P-protein using Lipofectamine 3000 (ThermoFisher) according to the manufacturer's instructions. Cells were treated 16 h post-transfection without or with IFNα (1000 U/mL, 30 min) before fixation (3.7% formaldehyde, 10 min) and permeabilization (90% methanol, 5 min). Cells were immunostained with rabbit anti-STAT1 (CST, Cat# 14994; 1:1000 overnight 4°C) followed by Alexa Fluor-568 conjugated goat anti-rabbit secondary antibody (ThermoFisher, Cat #A-11011; 1:1000 90 min RT). Coverslips mounted onto glass slides using Mowiol were imaged using a Leica SP5 microscope with 60 × oil immersion objective and images processed with FIJI software (Schindelin et al., 2012). Images are shown in Figure S5.

Protein Complementation Assay

HEK293-T cells seeded into 96-well plates were transfected 18 h later with 100 ng of Glu1 and Glu2 (Brunel et al., 2014) chimeric constructs, and 5 ng of pGL4.50 (Promega), which constitutively expresses firefly luciferase. Cells were treated without or with IFNα (1000 U/mL) 24 h post-transfection and *Gaussia* and firefly luciferase activities measured after a further 24 h using the *Renilla* and Firefly Luciferase Assay Systems (Promega), respectively. Gaussia-luciferase activity was normalized to firefly luciferase activity. Protein–protein interaction levels are expressed as normalized luminescence ratios (NLRs), according to the following formula (Cassonnet et al., 2011):

$$NLR = (Glu1A + Glu2B)/[(Glu1A + Glu2) + (Glu1 + Glu2B)] \quad (5)$$

where Glu1A and Glu2B are chimeric proteins, and Glu1 and Glu2 empty vectors.

Co-immunoprecipitation and immunoblotting

For co-immunoprecipitation (co-IP) assays, COS-7 cells seeded into 6-well trays were transfected to express GFP-fused P-proteins prior to treatment without or with 1000 U/mL IFNα 16 h post-transfection. At different time points post-treatment, cells were washed twice with PBS and harvested into 200 μL of cell lysis buffer (10 mM Tris-HCl, 150 mM NaCl, 0.5 mM EDTA, 0.5% NP-40, pH 7.5). Lysate was passed through a 27G needle 10 times, and incubated on ice (30 min) before centrifugation (12000 *g*, 10 min, 4°C).

10% of cleared lysate ('input' sample) was solubilised in SDS-PAGE loading buffer and the remainder subjected to co-IP using the GFP-Trap-MAG system (Chromotek) according to manufacturer's instructions, before elution using SDS-PAGE loading buffer. Input and co-IP samples were separated by SDS-PAGE before western blotting and analysis using mouse anti-pY-STAT1 (CST, cat. #9176), rabbit anti-STAT1 (CST, cat. #14994), and rabbit anti-GFP (Abcam, cat. #ab6556), followed by HRP-conjugated goat anti-mouse (Chemicon, cat. #A308P), or goat anti-rabbit secondary antibodies (Chemicon, cat. #AP307P) and detection using Western Lightening ECL reagents (Perkin Elmer) and a Gel Doc XR+Gel Documentation System.

Gel shift assay

PCR fragments (0.55 kb) containing 4 copies of M67 sequence (TTCCCGTAA) were obtained by PCR (Table S2) from the 4xM67 pTATA TK-luc (Walker et al., 2010) using OneTaq DNA Polymerase (NEB, catalog # M0482S). PCR was purified using Wizard® SV Gel and PCR Clean-up system.

For gel shift experiments, 200 ng of DNA were incubated in 15 μL of 50 mM Na_2HPO_4, 100 mM NaCl, and 2 mM DTT, pH 7.4 for 1 h at room temperature with recombinant protein (pY-STAT1, WT or mutant P-CTD, or pY-STAT1 pre-incubated with WT or mutant P-CTD at room temperature for 20 min). 3 μL of DNA loading dye (0.25% Orange-G and 50% glycerol in milli-Q water) was then added to each sample prior to electrophoresis on a 1.2% agarose gel. 2-log DNA ladder (NEB) was used to indicate the size of the bands. Gels were run in 1x TAE buffer (40 mM Tris, 1 mM EDTA, 20 mM glacial acetic acid) and 0.5x SYBR-safe (Invitrogen™, catalog #S33102) (140 V, 25 min) before imaging on a ChemiDoc™ MP Imaging system with Image Lab™ software.

Virus reverse genetics and titration

WT Tha and Tha-FD recombinant viruses (derived from the rabies strain 8743THA (EVAg collection, Ref-SKU: 014V-02106) isolated from a dog in Thailand) (Thongcharoen et al., 1990) were generated by inserting the complete virus genome into pSDI-Flash-HH-SC (Ghanem et al., 2012), and introducing mutations (Table S2) to the P gene using the Change-IT™ Multiple Mutation Site-Directed Mutagenesis Kit (Affymetrix), according to the manufacturer's instructions. Recombinant RABVs were rescued (Buchholz et al.,

1999), by transfection into BSR-T7 cells of the complete genome (2.5 μg), and plasmids N-pTIT (2.5 μg), P-pTIT (1.25 μg) and L-pTIT (1.25 μg) (Ben Khalifa et al., 2016). 6 days post-transfection, cells were serially passaged every three days. When 100% of the cells were infected, the supernatant was harvested and titrated on BSR cells. The infection was controlled by immunofluorescence using the FITC-conjugated anti-rabies virus nucleocapsid antibody (Biorad).

Titrations were performed on BSR cells by the fluorescent focus method (Rupprecht et al., 2019). 20 μL of serial dilutions (1 to 5) of virus were inoculated in duplicate on 50,000 BSR cells and incubated at 37°C. Forty h post-infection (p.i.) the medium was removed, the cells fixed with acetone (80%) and incubated with the FITC-conjugated anti-rabies virus nucleocapsid antibody (Biorad). The number of fluorescent foci was counted under a fluorescent microscope and the titer calculated in Fluorescent Focus units/ml (FFU/mL). To generate growth curves for recombinant viruses, each virus was inoculated on BSR cells at a MOI of 0.1 and supernatants recovered at 24 h, 48 h and 72 h p.i. for titration on BSR cells.

QUANTIFICATION AND STATISTICAL ANALYSIS

Statistical details of each experiment can be found in the figure legends. Prism version 7 or 8 software (Graphpad) was used for statistical analysis. To compare means of two samples, Student's t test (unpaired, two-tailed) was used to calculate p values; in Figure 6B, unpaired two-tailed t test with Welch's correction was used. To calculate p values for survival curves in Figure 6C the log-rank (Mantel-Cox) test was used.

DATA AND CODE AVAILABILITY

This study did not generate any unique datasets or code.